POLITECNICO DI TORINO

Department of Environment, Land and Infrastructure Engineering

Master of Science in Geoenergy and
Georesources Engineering

Surface Wave Attributes for Enhanced Near Surface Anomaly Detection

Supervisors:

Prof.Chiara Colombero
Prof.Farbod Khosro Anjom
Prof. Laura Valentina Socco

candidate:

Jawdat Abd Al Karim

March,2025

This page has intentionally been left blank.

ACKNOWLEDGEMENTS

ABSTRACT

The shallow subsurface is usually highly complex and characterized by significant heterogeneities, which are crucial to depict for successful subsurface imaging in various applications. These lateral variations, that can be often associated with seismic low-velocity zones, can either be a target of seismic investigation or an important constraint for accurate reconstruction of the seismic velocity model using surface wave analysis. Three seismic surface wave attributes that are energy, energy decay exponent and autospectrum, have been shown to be highly sensitive to lateral variations, specifically low velocity anomalies. The computations of these attributes provide lateral profiles that allow the position of the heterogeneities to be identified or cross sections with images of the attribute in the space-frequency domain. In this thesis, we propose a workflow for estimating depth of the anomalies using these surface wave attributes and spectral properties of 3 component data. The proposed methods are evaluated using two 3D synthetic data, and a field data set from a test site with known properties of heterogeneities. The methods, based on transformation into a depth and on H/V spectral ratio, show the ability to detect and estimate the depth of near-surface sharp lateral variations.

Table of Contents

LIST OF FIGURES

List of Figures

LIST OF FIGURES

List of Tables

1 Chapter 1: Introduction

Seismic attributes are quantitative measures estimated from seismic raw or processed data used to characterize specific properties of the subsurface. The primary objective of seismic data processing is to produce seismic sections and volumes to discover subsurface targets for scientific or business interests (Safitri et al., 2020). Processing seismic attributes makes the seismic data more interpretable, reducing the negative impacts of bandwidth limitations and the non-uniqueness of seismic images, noise, and artifacts. Seismic attributes are used for interpreting seismic reflection data in the context of reservoir exploration and characterisation, but for shallower applications this approach is not applied. Shallow subsurface may include heterogeneities with strong lateral contrast in physical and mechanical properties. These heterogeneities can be characterized by high or low seismic impedance. Fractures, faults, cavities, and embedded low velocity bodies are all examples of heterogeneities usually characterized by lower seismic impedance than the background formation (Colombero et al., 2019).At large scales, the distribution of near-surface velocity can be used to identify faults and structural elements, which is helpful for geological modelling and drilling safety in hydrocarbon exploration

The identification and imaging of these targets can be critical using classical exploration methods. The Use of Ray-based P and S-wave tomography may lead to erroneous determination of the location and depth of sharp variations due to insufficient ray coverage and intrinsic limitation of refracted rays in detecting low-velocity zones (Colombero et al., 2016). On the other hand, the use of surface wave methods in practice and research shows an increasing trend, which can be observed in various scientific papers, including those in geophysical, engineering, and seismological literature (Socco et al., 2010). Surface wave tests are a non-invasive geophysical method used to evaluate shear wave velocity models. These methods are sensitive to lateral variability, but the inversion applied to derive the velocity model tends to provide smooth models with low resolution for the detection of local heterogeneities.

1 INTRODUCTION

Several researchers have implemented methods to improve the lateral resolution of SW based methods. For instance, integrating the surface wave data and the analysis through the cross-correlation technique also increases the capability of characterizing the anomaly by providing enhanced lateral resolution and less impact from the presence of the noise (Samyn et al., 2012). To improve the capability of identifying lateral heterogeneities, researchers have identified attributes computed from the seismic records. Many numerical simulations, especially those using the finite element method, and lab-scale tests were conducted to identify perturbations caused by anomalies (Nasseri-Moghaddam et al., 2005). Bergamo and Socco (2014) introduced a set of attributes based on several energy attenuation or enhancement parameters that proved to be useful to identify local heterogeneities such as shallow expression of faults.

Colombero et al., (2019) improved the computation of surface wave attributes (energy, energy decay exponent, and autospectrum) proved to be effective in the location of several subsurface targets. In their work, the attributes are computed as a function of the wavelength of the propagating SW. Wavelength can be considered a proxy for depth, but a method to generate a depth image of the seismic anomaly is needed. In this thesis, we develop two imaging methods that can be applied to both 1C (one component – vertical component) data and 3C (3 component) data. Starting from the existing attribute computation algorithms, these methods transform the wavelength axis into a depth axis based on the estimate of SW phase velocity or on the spectral ratio method. We apply these methods to two 3D synthetic models and a real test dataset to evaluate their effectiveness in improving depth estimation accuracy. In Chapter 2, we provide the theoretical background on SW and its attributes. We show the main concepts that refer to Rayleigh waves, such as dispersion curves, wave propagation, and investigation depth. This chapter can be considered the basics for the methodology introduced later by explaining the physical principles that are essential to our approach for estimating the depth of near-surface heterogeneities.

In Chapter 3, we introduce the datasets used for evaluation, including two 3D synthetic models that simulate near-surface heterogeneities and the real test datasets from the CNR (National Research Council) test site (Torino, Italy), and we apply the attribute computation to the data.

1 INTRODUCTION

In Chapter 4, we describe the methodology developed in this thesis for estimating the depth of the detected heterogeneities based on SW attributes. We develop a new approach: the energy ratio, which is the ratio between the energy inside the anomaly and the energy of the background based on multidirectional measurements using 3C data. We also introduce another approach, the Horizontal-to-vertical (H/V) spectral ratio. This Chapter comprehensively explains the computational workflow used to extract meaningful subsurface information from seismic data.

Chapter 5 presents the results obtained for depth estimation to our models. Then, we evaluate the effectiveness of surface wave attributes in detecting and localizing anomalies. We then apply both energy ratio and H/V spectral ratio methods to estimate the depth of identified anomalies. The results are validated by comparing estimated depths to known values in synthetic models and existing information from the real dataset.

In Chapter 6, we drive conclusions, discuss the advantages and limitations of each approach in terms of accuracy and sensitivity to lateral variations, and discuss future development of the present work.

2 Chapter 2: Overview of Surface Waves & their Seismic Attributes

In this chapter, we briefly introduce the propagation of seismic waves, with a significant focus on SW (Surface Waves), their properties, and propagation characteristics. Then, we will introduce the concept of seismic attributes and how they help us identify sharp subsurface lateral heterogeneities.

2.1 Surface waves

When the energy is propagated through or along the surface of a medium, which comes from various sources that can be used at the surface, the periodic vibrational disturbance will occur, which will be called seismic waves. They are categorized into two types: waves propagating in all directions from the source and traveling through the earth's interior, called body waves, and waves traveling along the free surface, called surface waves.Surface Waves propagate parallel to the earth's surface and decay exponentially in depth. There are several types of SWs, such as Lamb, Love, Scholte, Rayleigh, etc. In this thesis, we will use Rayleigh waves.

Surface waves have many properties that make them particularly suitable for geometrical characterization. They have a much lower rate of geometric attenuation than body or bulk waves, and this is because the energy of body waves spreads in both horizontal and vertical directions, while for SW has a radiation pattern, as shown in Figure 2-1. directions, while for SW has a radiation pattern, as shown in Figure 2-1.
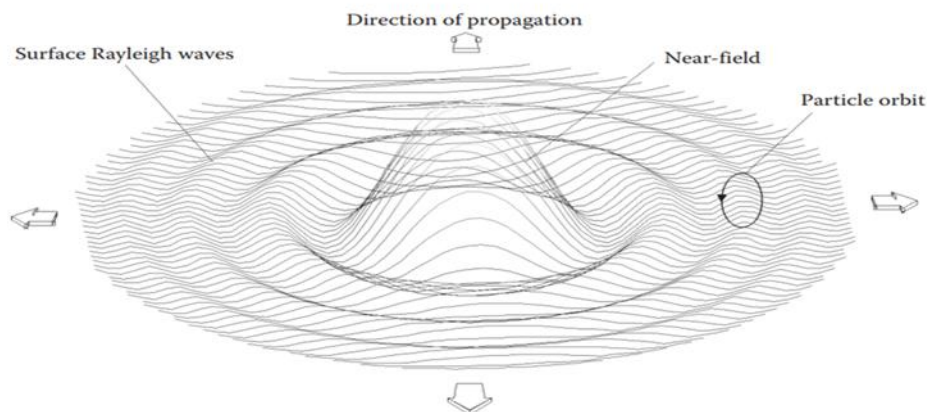
Figure 2-1: Radiation pattern of Rayleigh surface waves generated by a vertical point source.

2.2   Rayleigh wave Propagation

Rayleigh waves are named after the mathematician Lord John Strutt Rayleigh, who predicted this kind of wave (Strutt,1885). Rayleigh waves are a combination of longitudinal and vertically polarized transverse waves, Fig.2-2. The displacement field generated by a surface wave decays exponentially with depth since no energy is propagated in the interior of the half-space, and in that case, the strain energy will be limited within a depth of about a wavelength λ from the free boundary. So, Rayleigh waves with large wavelengths penetrate deep into the interior of a medium. To further understand, we can say that high-frequency waves are confined to shallow depths while low-frequency waves are limited to considerable depths.
.
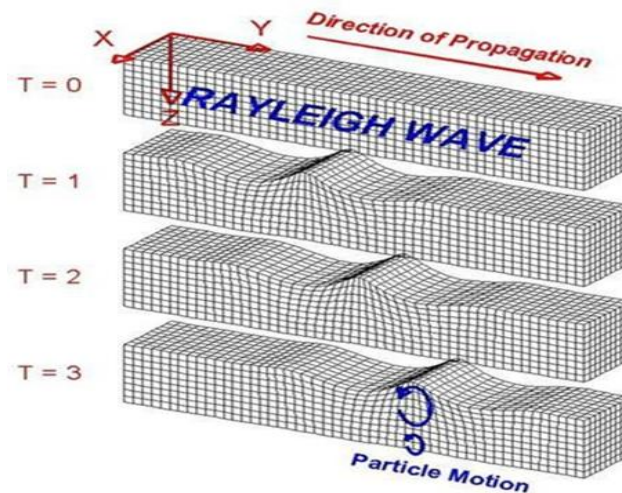
Figure 2-2: Direction of propagation and evolution of surface waves with time T: Rayleigh wave. X and Y are parallel to the surface while Z is the depth. Particles are represented by cubes in these two models (Braile 2006).

2.2.1 Geometric Dispersion

In a homogeneous, isotropic, linear elastic half-space, the velocity of a Rayleigh wave is a function of the mechanical properties and not a function of frequency. However, in vertically heterogeneous media, geometric dispersion occurs, resulting in a phase velocity for Rayleigh waves that becomes frequency-dependent.

Figure 2-3 shows a horizontally layered medium consisting of two layers overlying a half-space. On the left, where high frequency (i.e., short wavelength) is present, the particle motion is confined within about one wavelength from the free surface and occurs mainly in

layer 1, and the material properties of the layer control the velocity of the Rayleigh wave. However, when low frequency (i.e., long wavelength), the particle motion extends to greater depths, involving layers 1, 2, and part of layer 3. In that case, the Rayleigh wave velocity is controlled by the relative amount of particle motion occurring within each layer.
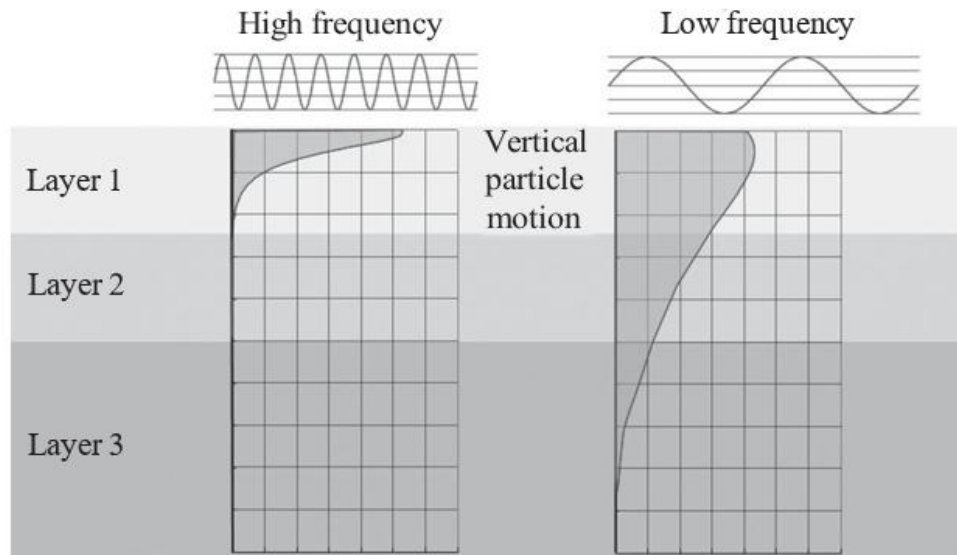
Figure 2-3:Geometric dispersion of Rayleigh waves: trends with depth of the vertical particle motion associated with the propagation of two harmonic waves in a layered medium.

The dispersive nature of Rayleigh waves, described by the dispersion curve (the relationship between Rayleigh phase velocity as a function of frequency, allows the shear wave velocity profile to be obtained for a specific site through the solution of an inverse problem. Thus, this dispersive nature of Rayleigh waves is used to characterize the interior of a medium.

Referring to Fig.2-4 (a), we can see that we have a model characterized by increasing stiffness with depth. As a result, the shear wave velocity of the second layer is higher than that of the first layer but lower than the velocity in the half-space below. In Fig. 2-4 (b), a high-frequency Rayleigh wave traveling in the top layer will have a propagation velocity slightly lower than the shear wave velocity of the first layer. On the other hand, in Fig.2-4 (c), a low-frequency wave will travel at a higher velocity because the underlying stiffer material also influences it.

Figure 2-4 (d) shows a plot of phase velocity versus wavelength, with an increasing trend for longer wavelengths. Fig.2-4 (e) shows the dispersion curve and the relationship between phase velocity and frequency. This curve is sensitive to the seismic properties of the medium, particularly to S-wave velocity and can be then used into an inverse problem to estimate a VS profile.
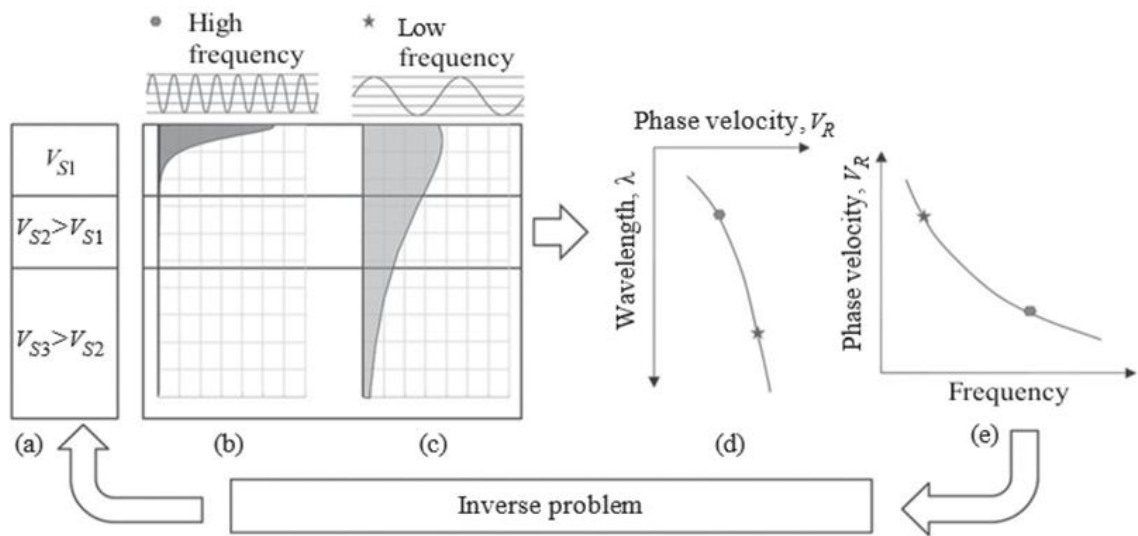
Figure 2-4:Parameter identification based on geometric dispersion.

In the scheme described in figure 2-4, the reference model for SW propagation and SW inverse problem solution is a 1D model, where the properties are considered laterally invariant. In the real world, the subsurface is highly heterogeneous and it is therefore important to account for lateral variability.

2.2.2 Investigation Depth

The investigation depth of SW is related to the thickness of the layer within which the wavefield propagates. As explained in section 2.2.1, different harmonics, hence different wavelengths, propagate at different depths. While in homogeneous half space the displacement distribution with depth makes it easy to define an approximated relation between the wavelength and the investigation depth, for layered media the displacement pattern in the subsurface becomes more complex. Nevertheless, several researchers have proposed approximated relationships to transform the propagating wavelengths directly into a depth.

To prevent subsidence related to infrastructure damage by identifying the voids beneath construction sites and urban sites, a research based on Rayleigh wave attenuation analysis (AARW) to detect the underground voids and estimating their embedment depth (Nasseri-Moghaddam et al., 2005). This method uses numerical simulations, and it is based on the frequency attenuation of Rayleigh waves. The results indicate that voids' embedment depth is approximately 0.5 to 1 time the wavelength of Rayleigh waves.

Begramo and Socco investigated methods in 2014 to detect sharp lateral in subsurface environments using surface wave propagation analysis. They used both synthetic and field data to validate their approach, in which the results show that the sharp discontinuities lead to interference between the incident and reflected wave. The findings also show that the depth of the discontinuities is approximately equal to the wavelength of the propagating Rayleigh waves.

Autospectrum calculations and 2D Fourier Transforms were applied to detect energy variations caused by cracks and to analyze Rayleigh wave behavior in cracked concrete members (Zerwer et al., 2005). A strong reflection occurs at the crack location and these reflections can be used to estimate crack depth. The key observation in this study is that Rayleigh waves don't propagate beyond half the beam depth and in that case the maximum detection depth is approximately half of the wavelength.

2.3 Surface Wave Attributes

2.3.1 Energy attribute

Energy attribute was proposed by Nasseri-Moghaddam et al. (2005) and applied to single-fold data to determine the location of underground cavities by observing energy fluctuations in the proximity of voids. In 2014, Bergamo and Socco applied this method to synthetic and real data of a fault zone and observed a sharp energy decay at the discontinuity location. Later, the same method was adopted for locating open fractures within a granitic rock mass, identifying marked energy concentrations at the discontinuity interfaces (Colombero et al., 2017)

The energy will be the first attribute used to detect the location of sharp variations in the subsurface. It computes the energy of the seismic traces acquired along a line. According to Nasseri-Moghaddam et al. (2005), the energy E_i is computed for each receiver i as the sum of the squared amplitudes $A_{f,i}$ at each frequency f, as shown in equation (3.1):

$$E_i = \sum_f \left| A_{f,i} \right|^2 r_i. \qquad (3.1)$$

The geometrical spreading will be compensated, and the results will be multiplied by a gain factor considering the distance r_i , which is the distance between the source and the receiver. By following the workflow of Colombero et al. (2019), for each common-shot gather (CSG), the resulting E_i values are normalized to the maximum E_i.

Before visualizing in $E - r$ (energy-distance) plots, the results for each source along the line are stacked and renormalized to the global maximum along the seismic line. These plots are then used to identify energy concentrations (energy maxima) or energy decay (energy minima), which can potentially identify subsurface lateral changes.

2.3.2 Energy decay exponent Attribute

Attenuation analysis of Rayleigh waves (AARW) was developed by Nasseri-Moghaddam et al. (2005) to detect underground cavities' location and embedment depth using SWs. Later, Bergamo and Socco (2014) extended this method to multifold data to automate the process and benefit from the redundancy of seismic data. This approach increases readability

and reduces uncertainties. Later, the method was tested using both synthetic and field data sets (Colombero et al., 2019). A new parameter, the energy decay exponent, was defined according to the following equation (3.2):

$$\frac{E_{i+1}}{E_i} = \left(\frac{r_{i+1}}{r_i}\right)^{-\gamma}, \qquad\qquad (3.2)$$

Where E_{i+1} and E_i are the energy values computed at two receivers with offsets r_{i+1} and r_i, respectively, the distance between the source and receiver. The energy decay exponent value γ may be positive or negative and sometimes equal to zero. In the case of a homogeneous medium, after recovering the geometric spreading, the energy decay exponent will be equal to zero. If the energy decay exponent exceeds zero, it indicates energy decay due to back reflections. Conversely, if the energy decay exponent is less than zero, it indicates energy concentration due to energy trapping within heterogeneity.

For each CSG, a moving window is shifted along the traces to calculate the energy decay exponent. In the case of a logarithmic scale, the energy decay exponent will be the slope in the $E - r$ plot according to the following equation (3.3):

$$log\left(\frac{E_{i+1}}{E_i}\right) = -\gamma\, log\left(\frac{r_{i+1}}{r_i}\right). \qquad\qquad (3.3)$$

After the energy decay exponent values obtained from different shots for each window are averaged for positive and negative offsets, the oscillations of the energy decay exponent obtained are shown due to sharp lateral variations in the subsurface, especially when the graphs exhibit opposite trends for positive and negative offsets caused by the discontinuity position.

2.3.3 Autospectrum Attribute

The autospectrum attribute was developed by Zerwer et al. (2005) for detecting cracks within concrete beams. The autospectral density G_i of a seismic trace $Y_i(t)$ can be defined as the sum of the squares of both real and imaginary parts of the discrete Fourier transform $Y_i(f)$ of the signal. The autospectrum is computed according to equation (3.4):

$$G_i(f) = \{Re|Y_i(f)|\}^2 + \{Im|Y_i(f)|\}^2. \qquad (3.4)$$

Computing G_i for a CSG is the same way to show the energy content of a seismogram as a function of the frequency and offset. Later, this method was applied to multifold data, the autospectral density of the traces was computed, and geometric spreading was recovered to remove the effect of the source position on the final plot. This plot is the normalized plot of the stacked autospectral to increase the readability of the data and thus is used to identify anomalies related to the discontinuity (Colombero et al., 2019)

3 Chapter 3: Data

To test depth estimation methods, we used three datasets: two are synthetic data obtained through numerical simulations, and one is a field dataset acquired over a well-known test site.

The synthetic data aim to assess the capability to image the target heterogeneity in two different conditions: a low velocity anomaly that emerges up to the surface and a low velocity anomaly that is embedded at a certain depth below the ground surface. In both cases, the background presents a velocity gradient. Similar models were already analyzed by Colombero et al. (2019), but the simulation was carried out in 2D condition. In the present work we used the SOFI3D model, a 3D numerical solver for seismic data simulation that uses FD (Finite Difference) to simulate viscoelastic media. The number of cells used is 512 cells in the X direction and 256 cells used in both the Y and Z directions. The distance between the 2 cells is 10 cm. Ten damping cells at each corner of the model, and we consider a free surface on the top.

3.1 Synthetic Model A

The geometry of the target and seismic layout for synthetic model A shown in Fig.3-1, Model A is a layered system with a low-velocity anomaly in the center and P wave velocity model shown in Fig.3-2. A synthetic array of 61 geophones (G1 to G61) with a spacing of 0.5 meters was defined for positions between 10 m and 40 m in the X direction. Four sources' locations (S1 to S4) were assumed along the seismic line, with S1 at 10 m, S2 at 20 m, S3 at 30 m, and the last source at 40 m. The source is vertical, and the wavelet was defined as a 60 Hz Ricker wavelet. The Record length and sample rate in dataset simulation were equal to 1 s and 0.5 ms, respectively. The simulation led to 3 records for each source position, one for vertical component (y), one for the horizontal component in line with the receivers (x), and one for the horizontal component orthogonal to the receiver line (z).

3 DATA
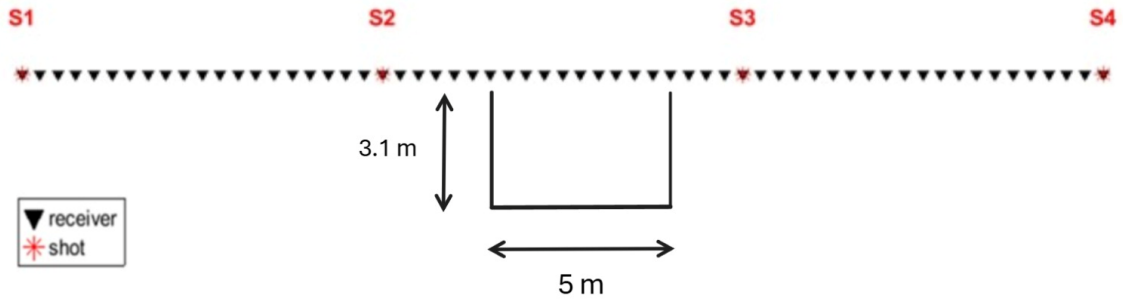
Figure 3-1: The geometry of the target and seismic layout for model A.
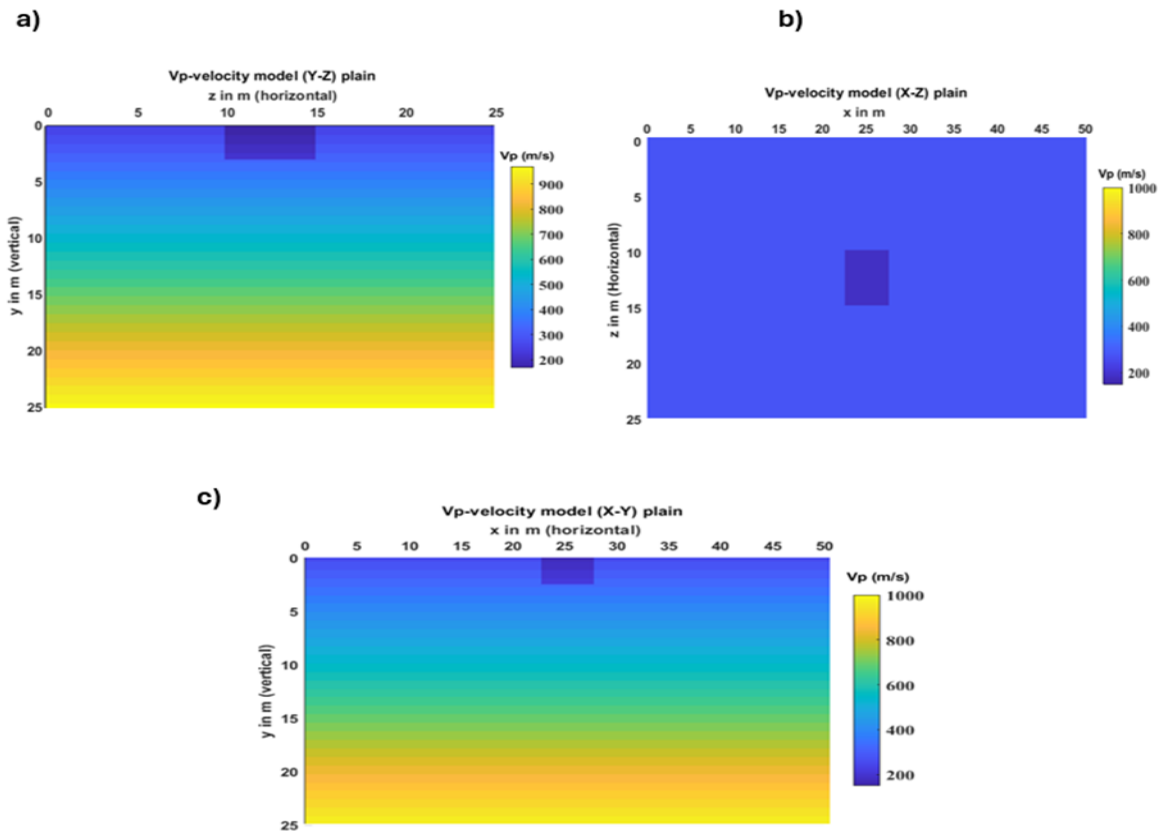
Figure 3-2: Vp-velocity model for synthetic model A a) Y-Z plain b) X-Z plain c) X-Y plain.

3 DATA

Figures 3-3,3-4 and 3-5 represent the synthetic seismograms for Shot 2 at 20 m in different components. From these seismograms, we can see the back reflections (R) from the boundaries of the anomaly.
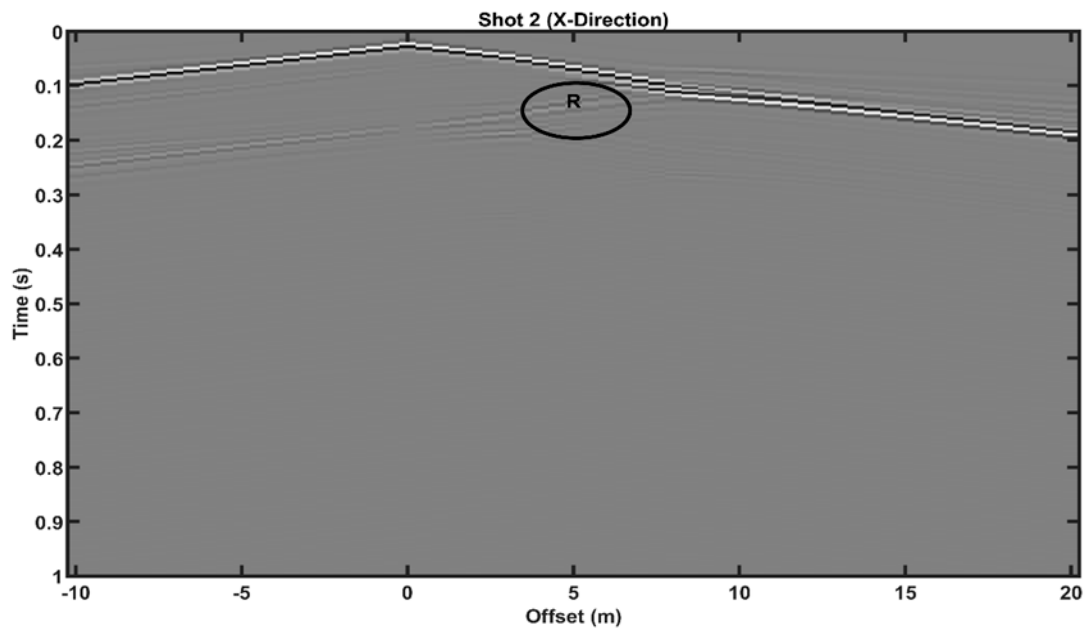
Figure 3-3: Synthetic seismograms for model A (shot 2 X-Component).
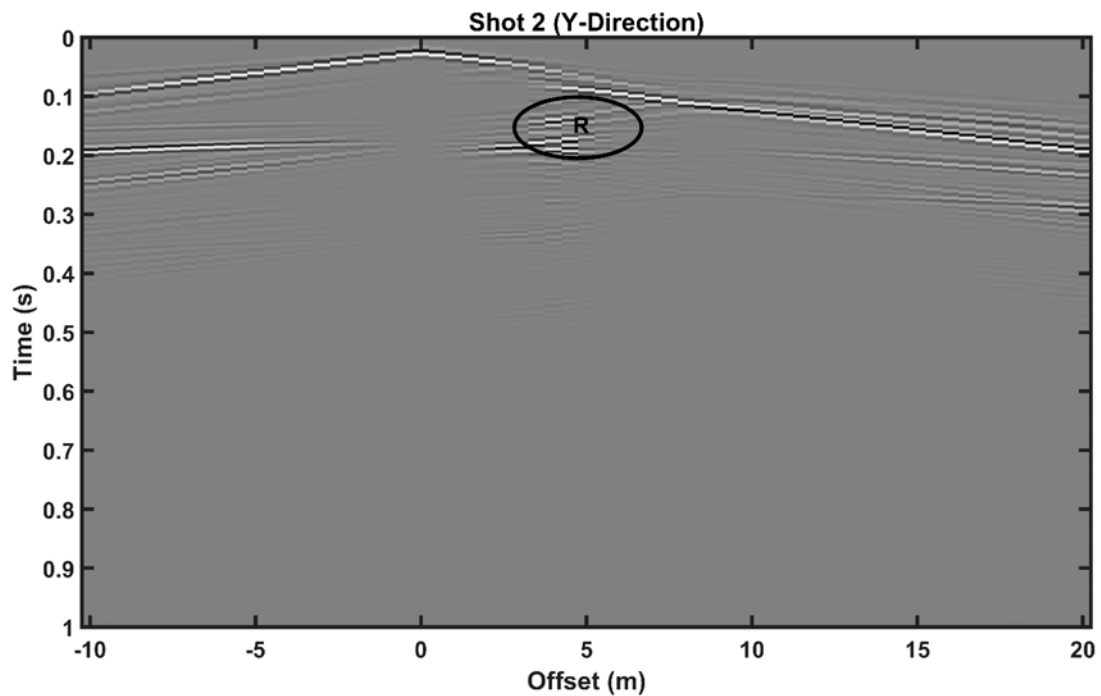
Figure 3-4: Synthetic seismograms for model A (shot 2 Y-Component).
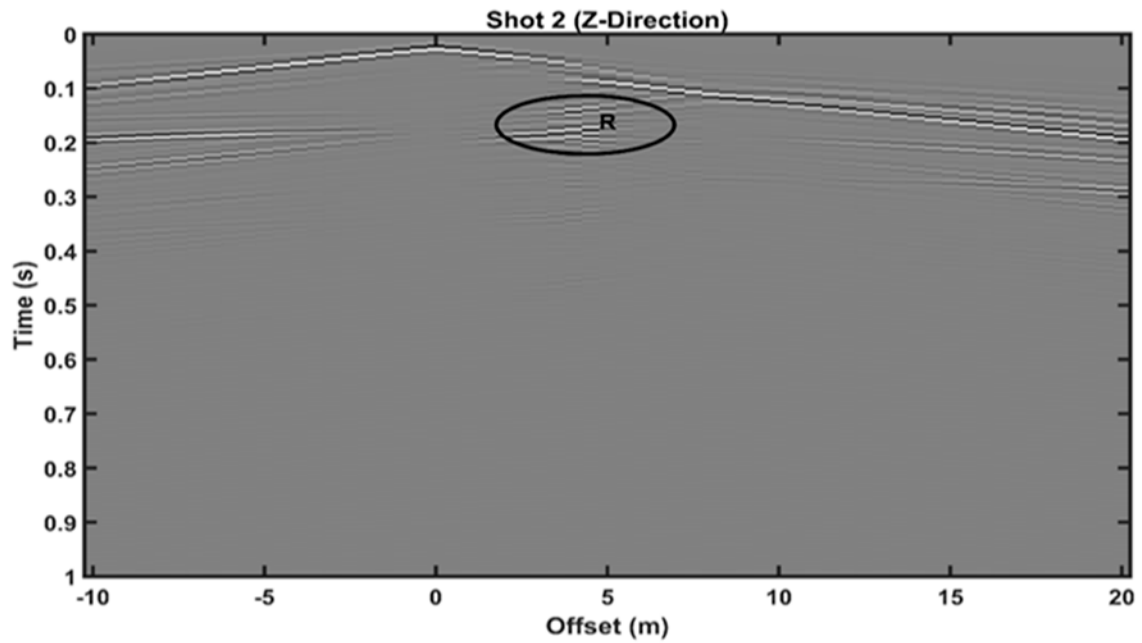
Figure 3-5: Synthetic seismograms for model A (shot 2 Z-Component).

3.2 Synthetic Model B

Figures 3-6 and 3-7 show the geometrical layout and Vp velocity model, respectively, for model B, which includes an embedded target of depth 5 m from the surface.
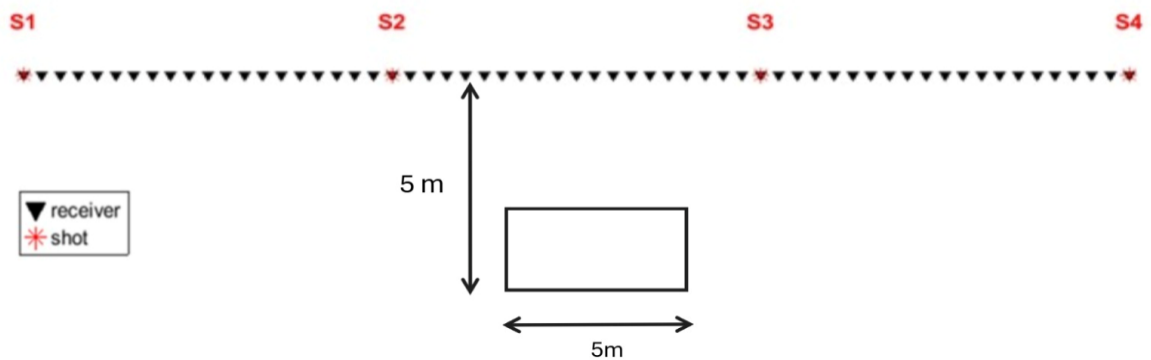
Figure 3-6:The geometry of the target and seismic layout for model B.
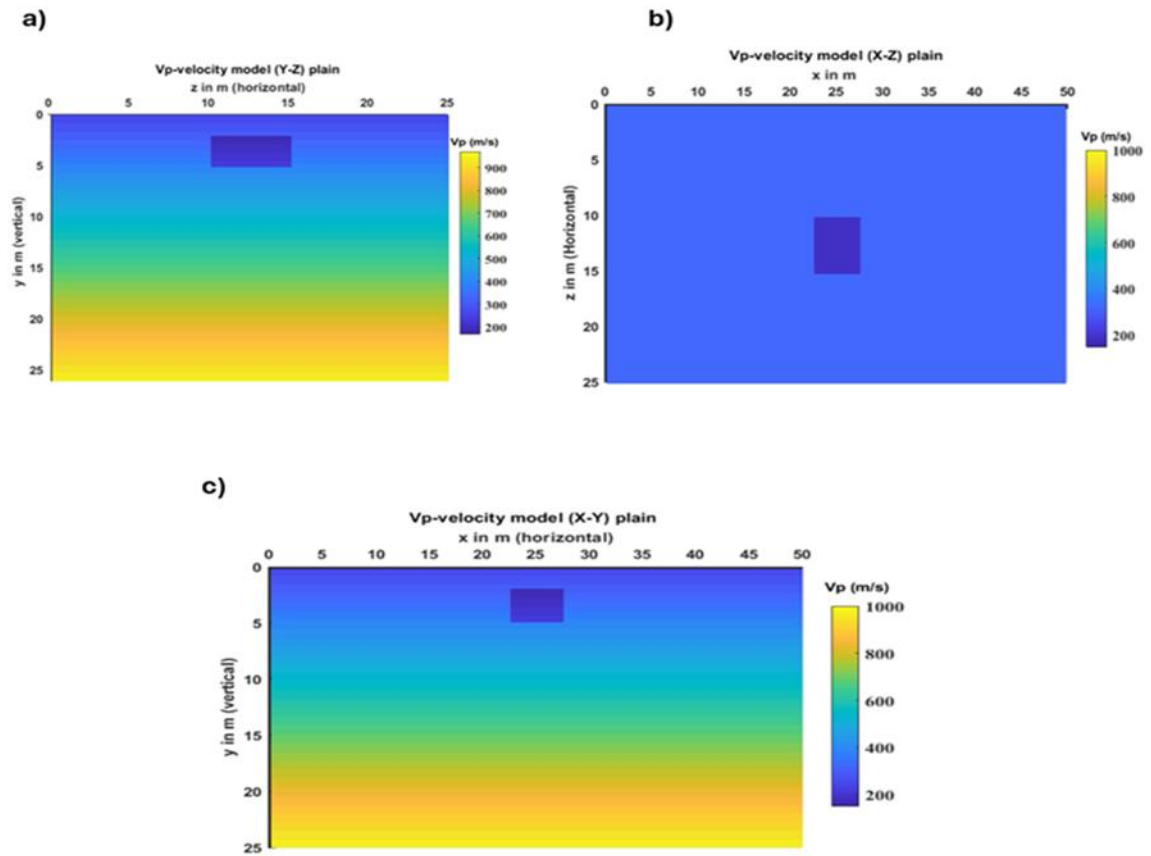
Figure 3-7:Vp-velocity model for synthetic model B a) Y-Z plain b) X-Z plain c) X-Y plain

Figures 3-8,3-9 and 3-10 represent the synthetic seismograms for Shot 2 at 20 m in different components.
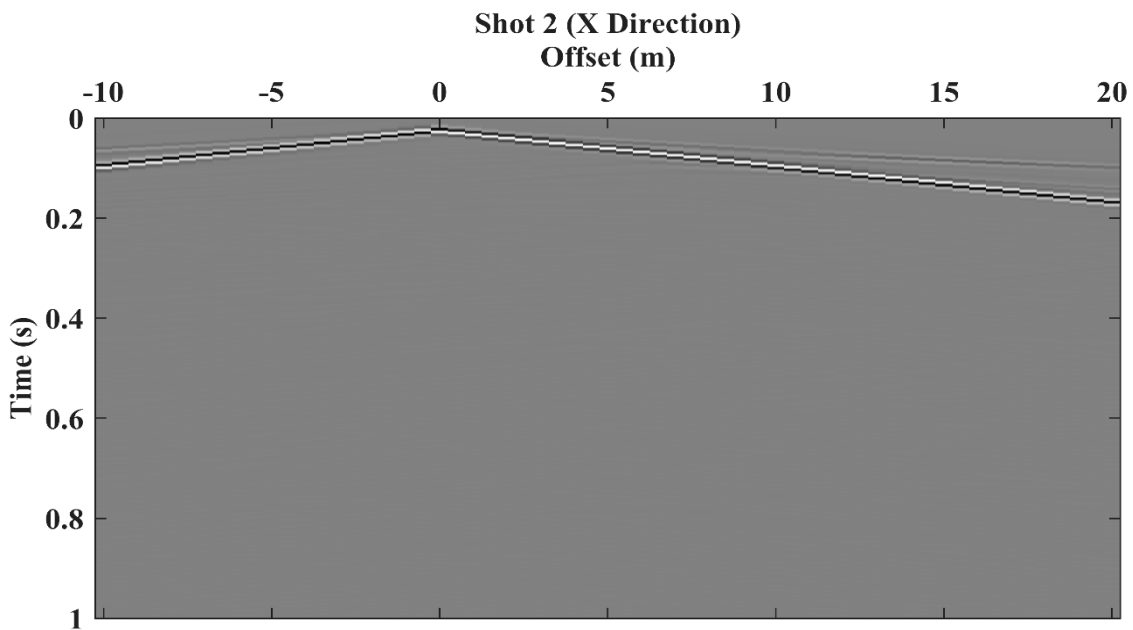
Figure 3-8:Synthetic seismograms for model B (shot 2 X-Component).

Shot 2 (Y Direction)
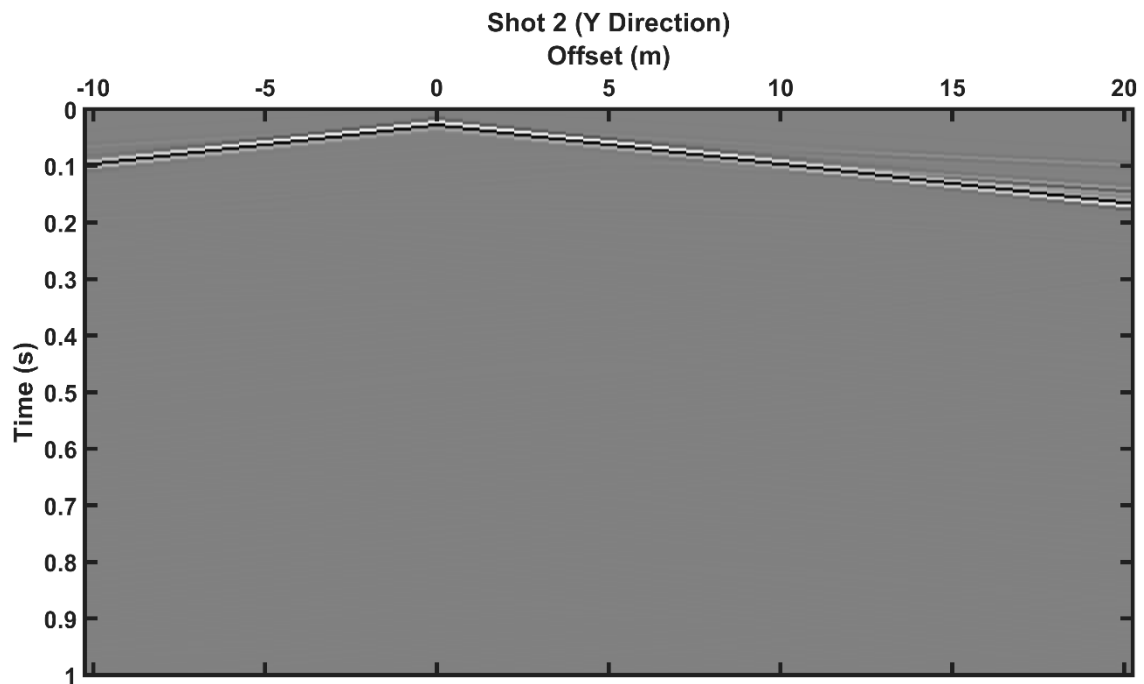
Figure 3-9:Synthetic seismograms for model B (shot 2 Y-Component).

Shot 2 (Z Direction)
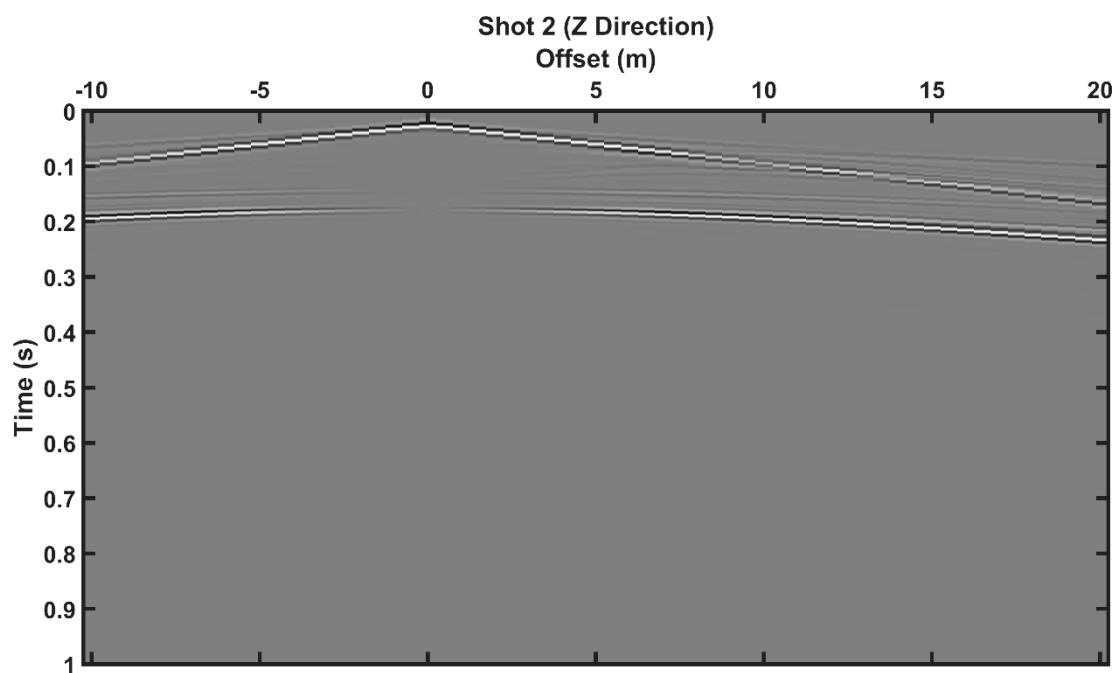
Figure 3-10:Synthetic seismograms for model B (shot 2 Z-Component).

3.3 Real Case Studies: CNR Test Site

At CNR (National Research Council) headquarters in Torino Fig.3-11 (a) and 3-12 (b), an artificial target was built in a flat area characterized by a shallow soil layer overlapping a thick sequence of alluvial deposits of the river plain, mainly composed of gravels with a silty matrix. Fig.3-11 (c), a square area of length 5 m and width 5 m was filled with loose sand, and this void had a depth of approximately 2.5 m. A seismic line of 30 geophones (3C) at 0.75 m spacing was deployed on site (total length = 21.7 m) with the sandbox in the center of the acquisition line. Nine shots (30 kg Weight drop) were struck at the line ends and along the array. The first two shots were located at 5 m and 2 m before the first receiver (G1), and the last two were located at 23.5 m and 26.5 m after the last receiver (G30), whereas the remaining shots were evenly spaced along the seismic line. Traces were recorded at a 1 ms sampling rate.
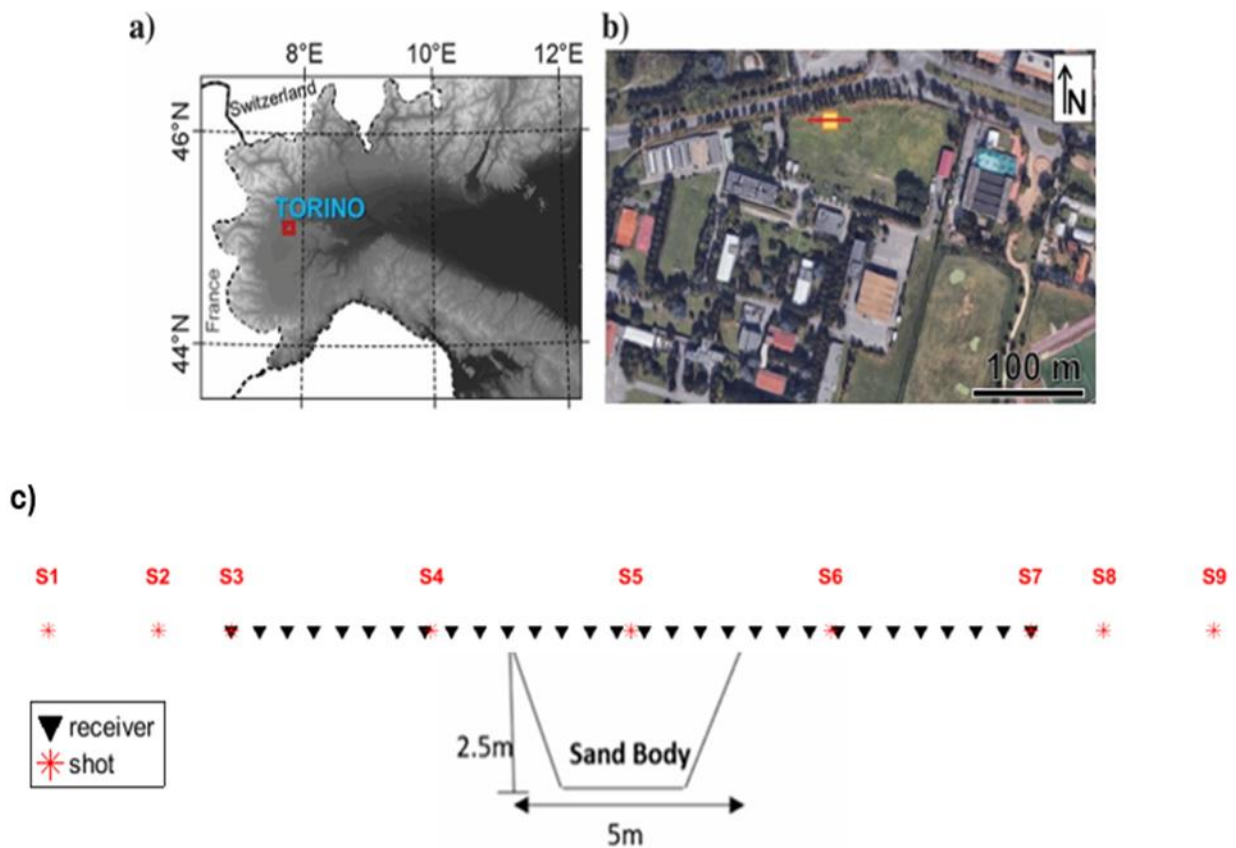
Figure 3-11: The CNR test site. (a) Geographic location. (b) Aerial view of the site with the location of the sandbox (the yellow square) and the seismic array (the red line). (c) The geometry of the target and seismic layout (Colombero et al., 2019).

Figure 3-12: Geophysical survey setup at CNR site.

Figures 3-13,3-14, and 3-15 represent the seismograms of the CNR site for Shot 7 at 22 m in different components.
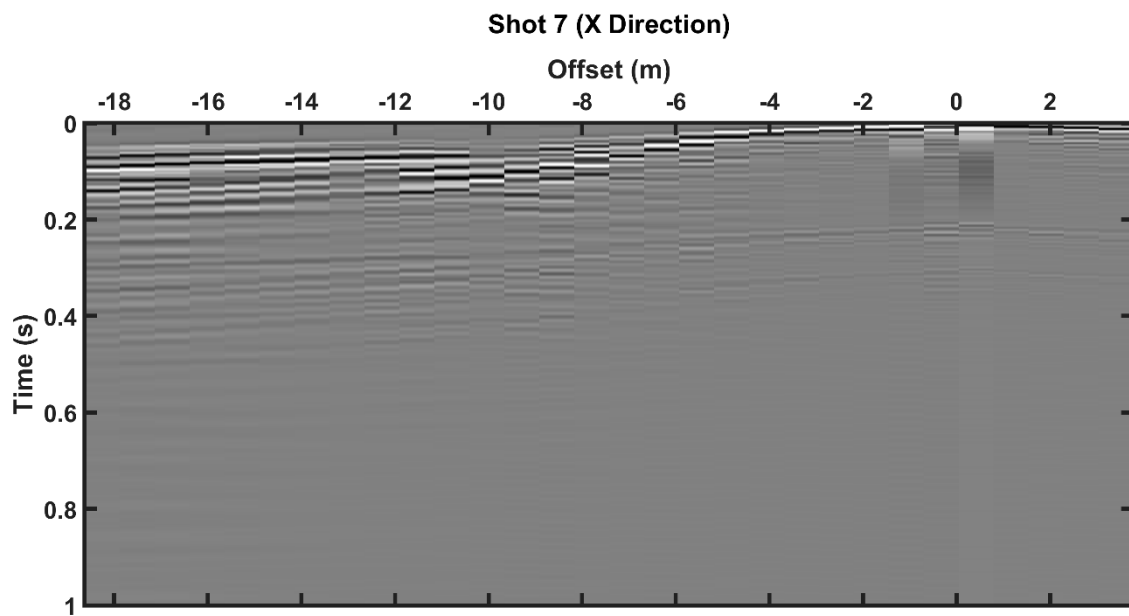
Figure 3-13:Synthetic seismograms for CNR (shot 7 X-Component).
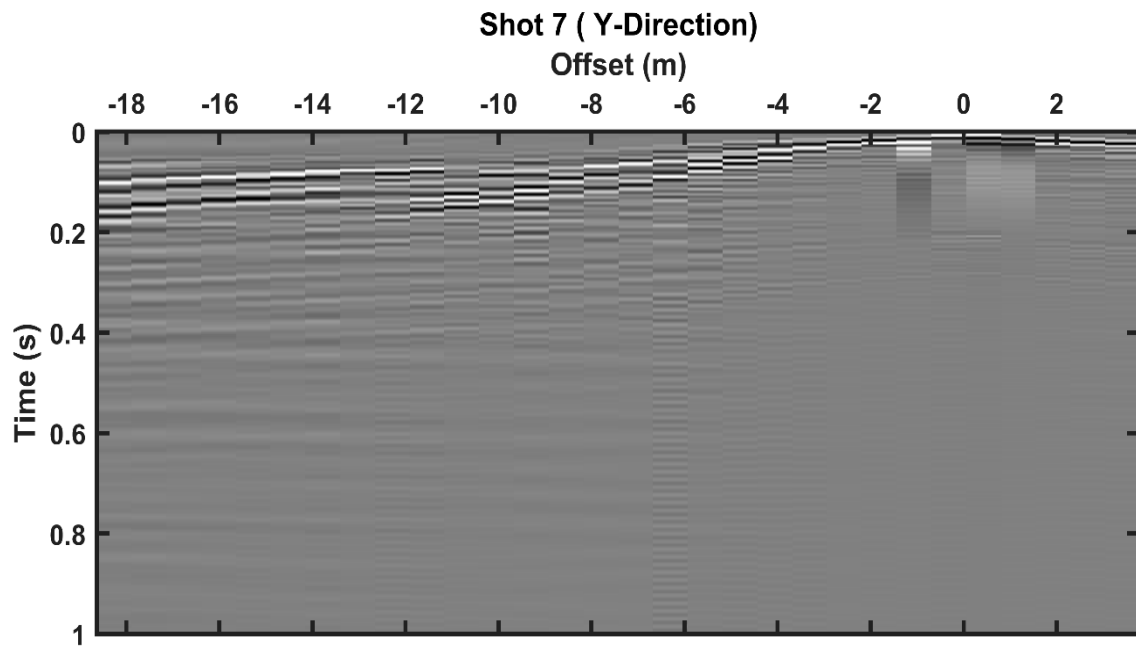
Figure 3-14:Synthetic seismograms for CNR site (shot 7 Y-Component).
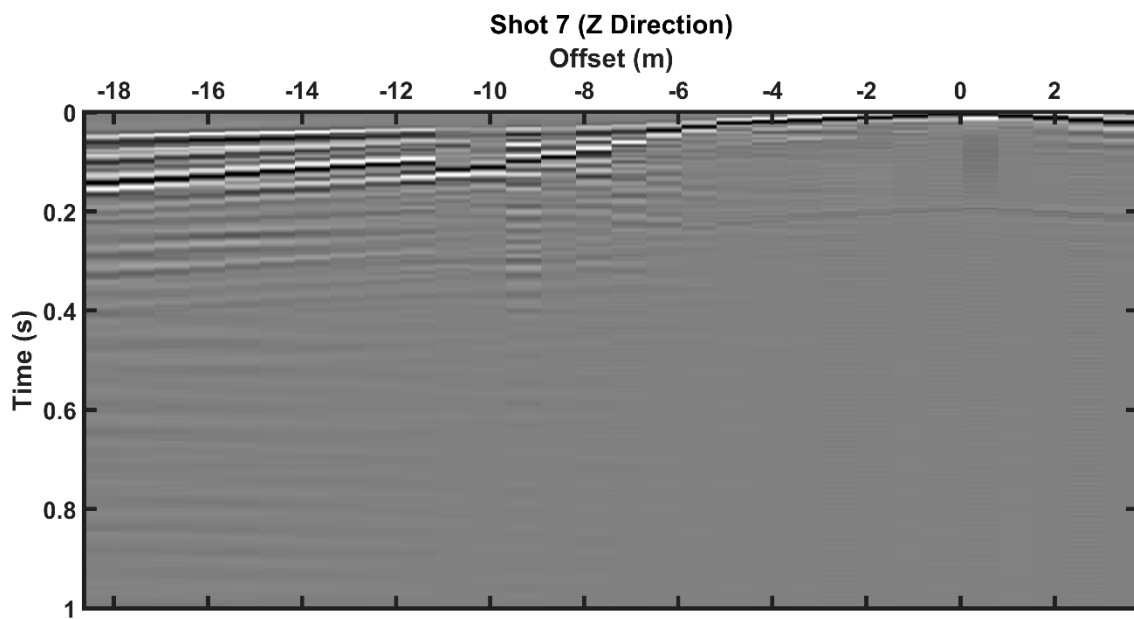
Figure 3-15: Synthetic seismograms for CNR site (shot 7 Z-Component).

3.4 Detection and Spatial localization of Heterogeneity

We use the MATLAB code Colombero et al. (2019) developed to compute the attributes of energy, energy decay exponent, and autospectrum. The flowchart in Fig.3-16 highlights the steps from the initialization step to the end, which includes results storing and visualization. It starts by defining parameters such as the minimum and maximum frequency, in our case, all the simulations were conducted with a frequency bandwidth between 5 Hz and 100 Hz representing the minimum frequency (min) and the maximum frequency (max), respectively. Also, the window size (receiver) was set to four (i.e., the portion of the signal analyzed in one "step" of the analysis), and the window step (receiver) was set to one (i.e., the distance the window moves after each analysis). Then, the preprocessing step is performed, in which the algorithm removes the mean and collects details regarding geometrical information, such as inter-receiver spacing and source positions. The Fourier Transform is applied to convert the traces from time domain into frequency domain, enabling us to compute surface wave attributes such as the autospectrum. After that, spatial windowing is implemented to help estimate the energy decay exponent attribute. Finally, stacking and normalization are performed for all attributes before sorting and visualization.
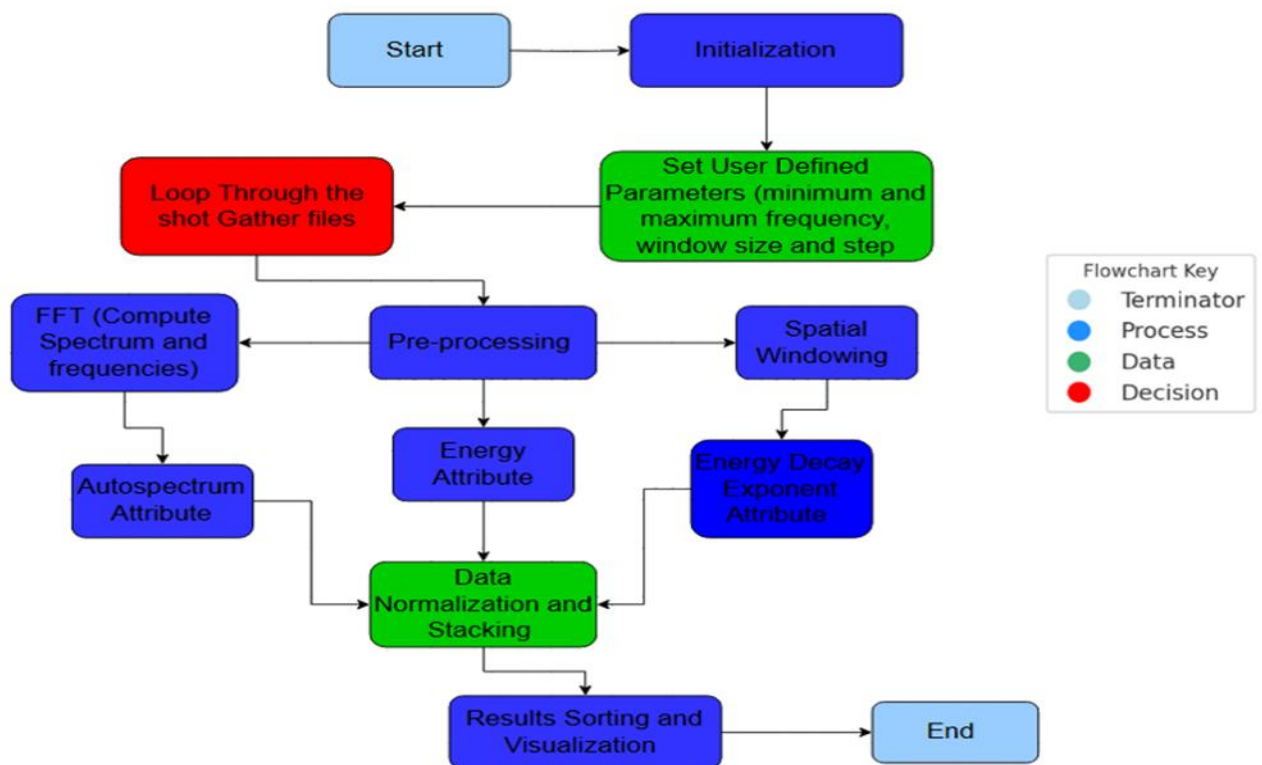
Figure 3-16: Algorithmic Workflow for Surface Wave Attribute Extraction and Visualization in MATLAB.

3 DATA

The normalized stacked energy results show apparent energy concentration within the anomaly zone, especially for synthetic model A Fig.3-17 and the CNR data Fig.3-19. In the records corresponding to all components, we can detect the boundaries of the target. Model A's anomaly boundaries range from 23 m to 28 m (width=5 m); for the CNR site, the boundaries range from 8 m to 13 m (width=5 m). For the synthetic model B (figure 3-18), we can see the effects of the source, especially in the Z component, and we can see the energy decay between 23 m and 28 m; in that case, we will consider it as the spatial boundaries for the anomaly.
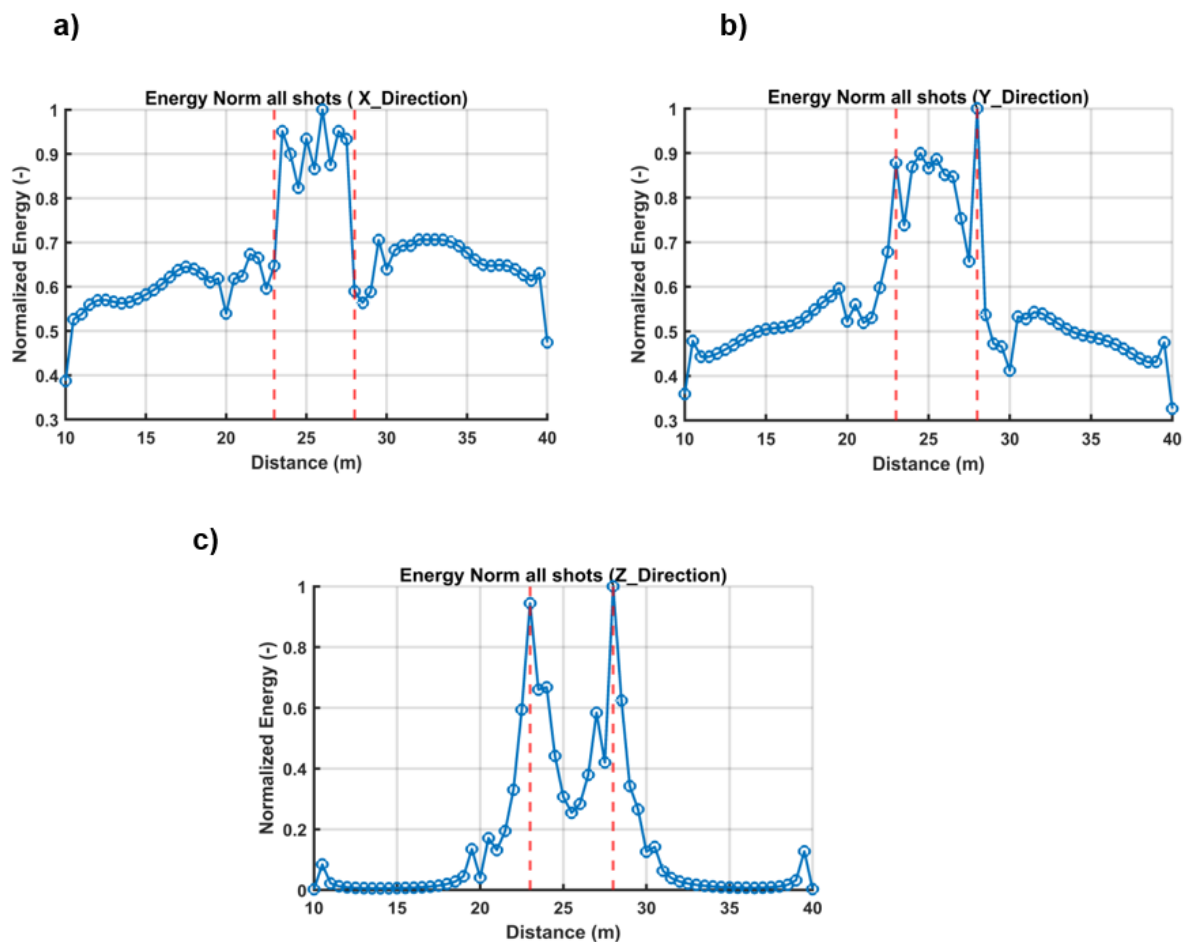
Figure 3-17: Normalized Stacked Energy for model A a) X-Component b) Y-Component c) Z-Component.
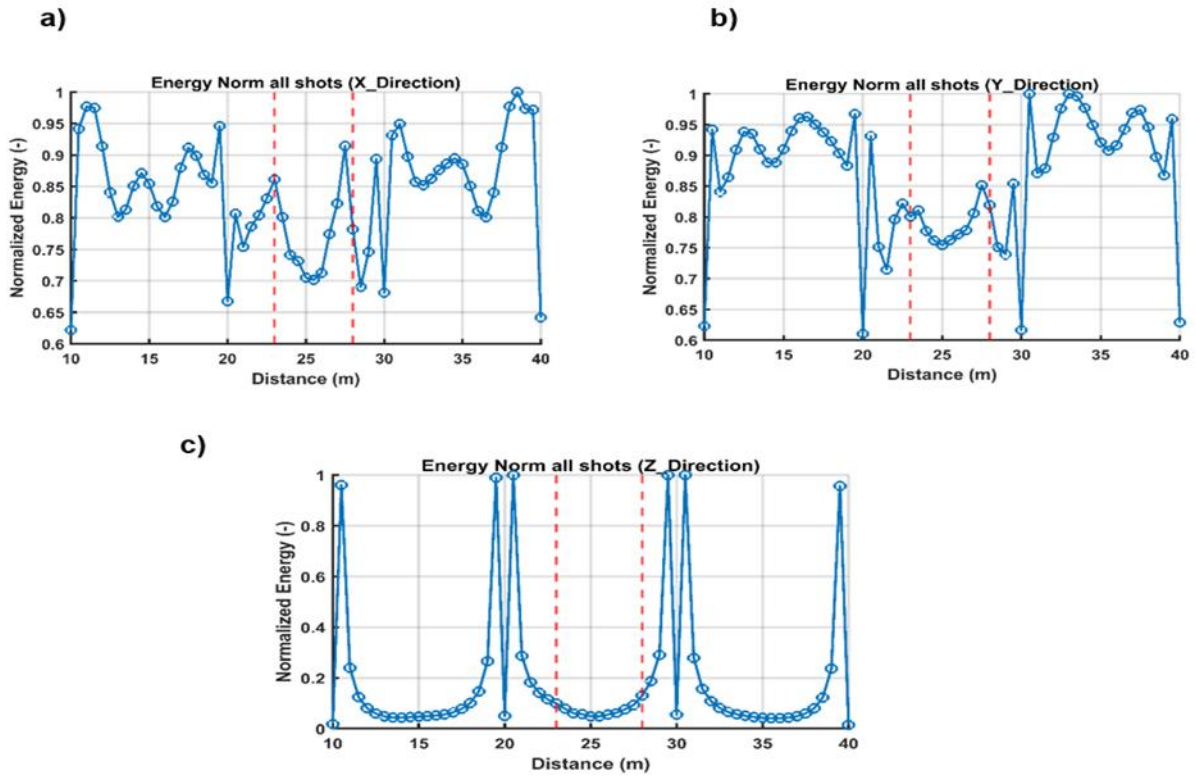
Figure 3-18: Normalized Stacked Energy for model B a) X-Component b) Y-Component c) Z-Component.
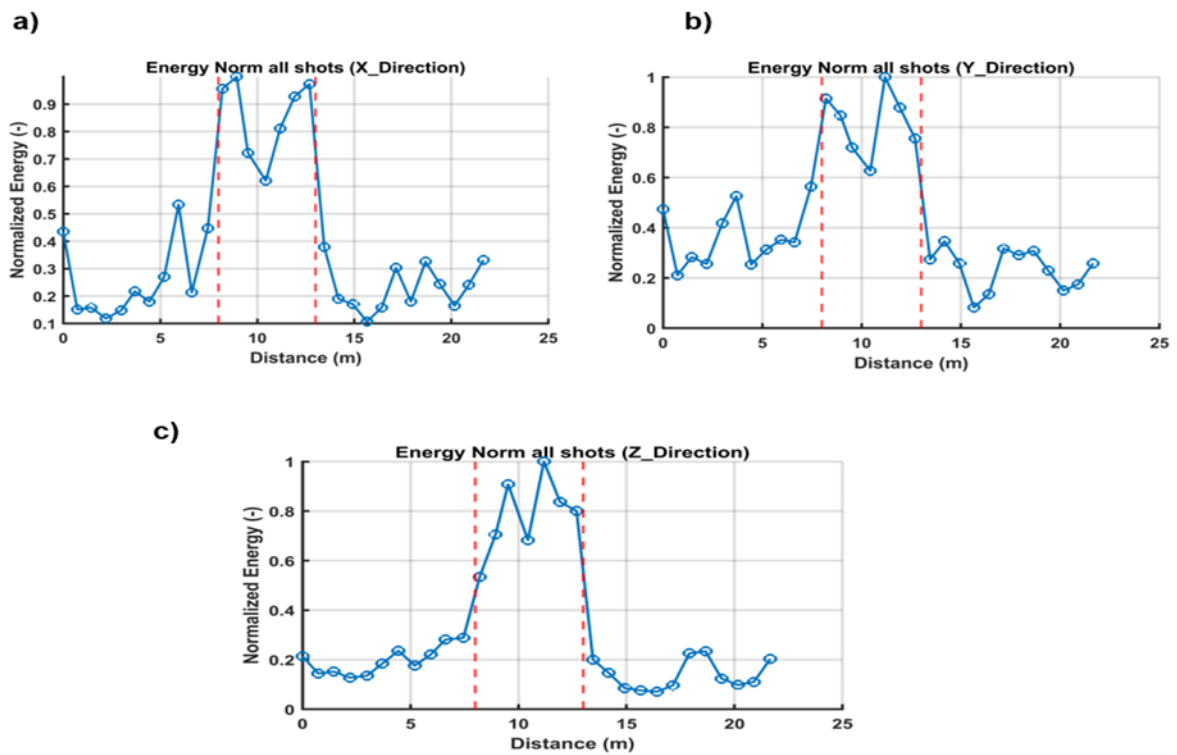
Figure 3-19: Normalized Stacked Energy for CNR site a) X-Component b) Y-Component c) Z-Component.

In the following, we present the results of applying the energy decay exponent method to both synthetic models (A & B) in Fig.3-20 and 3-21, respectively, and Fig.3-22 for the CNR site to the records of all the components (X, Y, and Z). We plot the $-\gamma$ as a function of distance, the maxima refer to energy concentration and the minima refer to energy decay. The energy concentration can be seen clearly at the boundaries of the anomaly. The peak amplitude for the contrast between positive and negative offset depends on the contrast between the target's velocity and the background. These results obtained are sufficient to locate laterally the anomaly.

a)

b)

c)
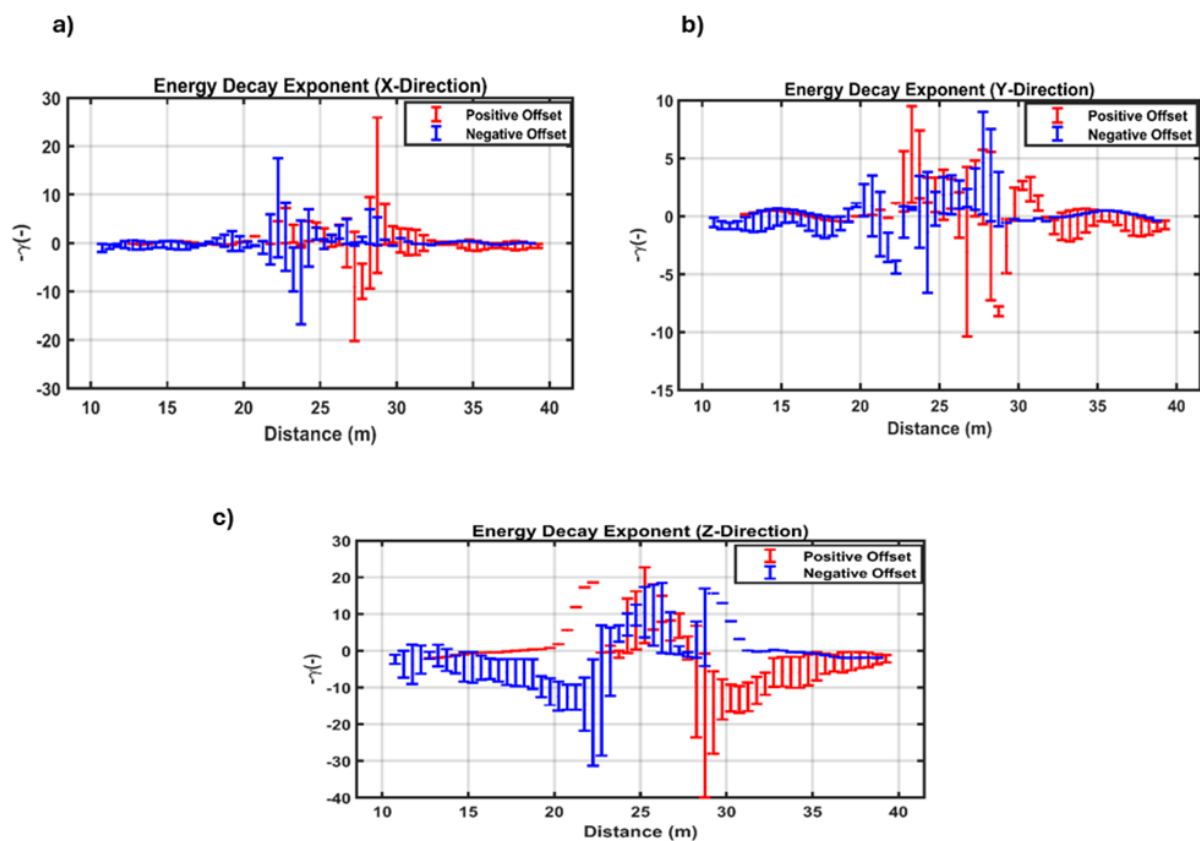
Figure 3-20: Energy Decay Exponent Results for Synthetic Model A a) X-Component b) Y-Component c) Z-Component.
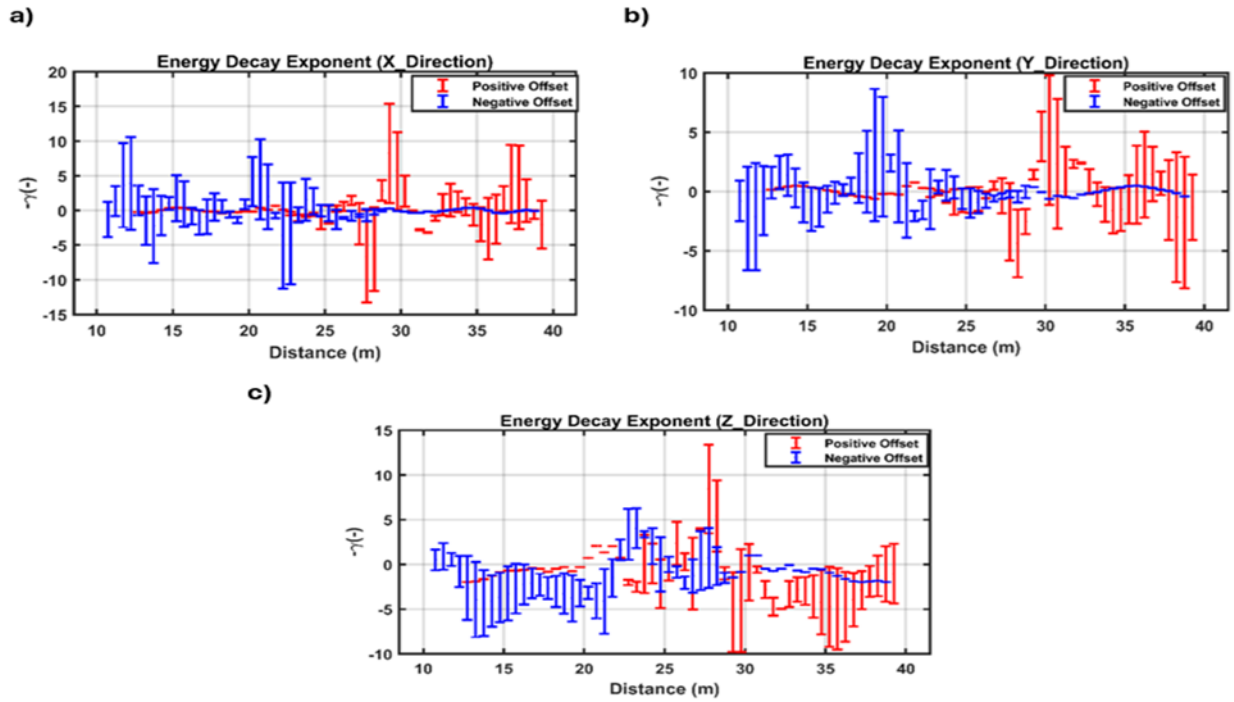
Figure 3-21: Energy Decay exponent results for model B a) X-Component b) Y-Component c) Z-Component.
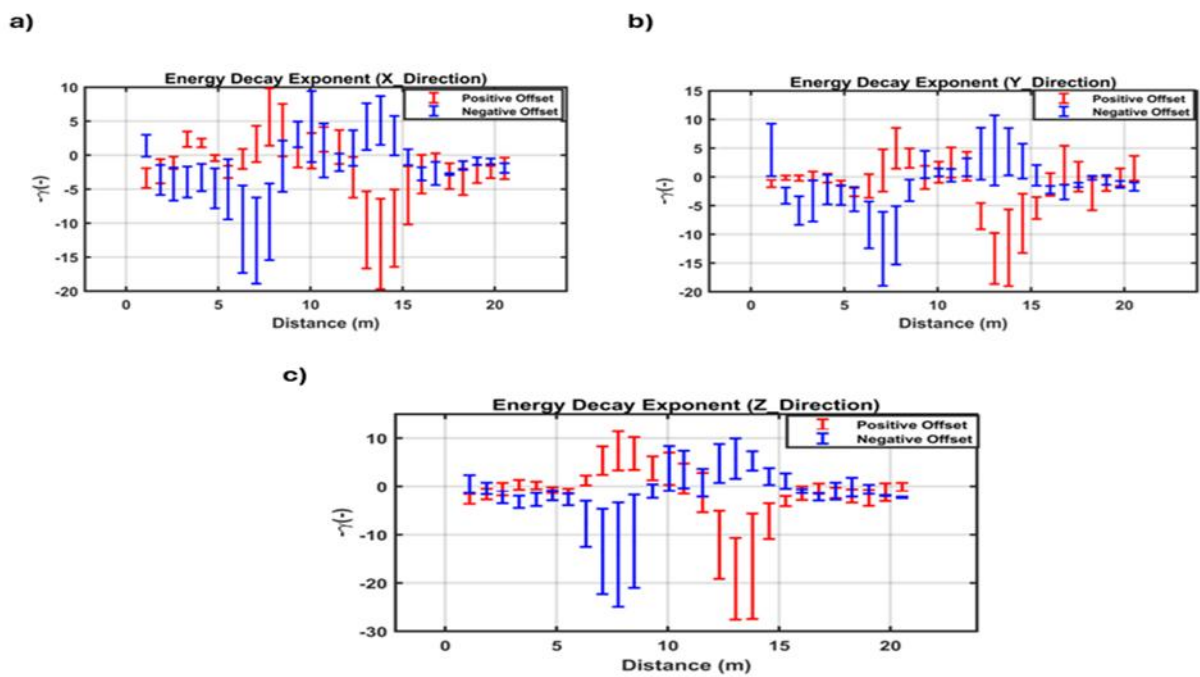
Figure 3-22: Energy Decay exponent results for CNR site a) X-Component b) Y-Component c) Z-Component.

3 DATA

We show the results for autospectrum plots in Fig.3-23 for model A and Fig.3-24 for model B. The anomaly is correctly located and imagined for model A and CNR site Fig.3-25, especially for the X and Y components where we can see high autospectral values within the target. While the results were obtained for model B, the plots did not detect the target, and we could not identify the anomaly's location and shape.

a)

b)

c)
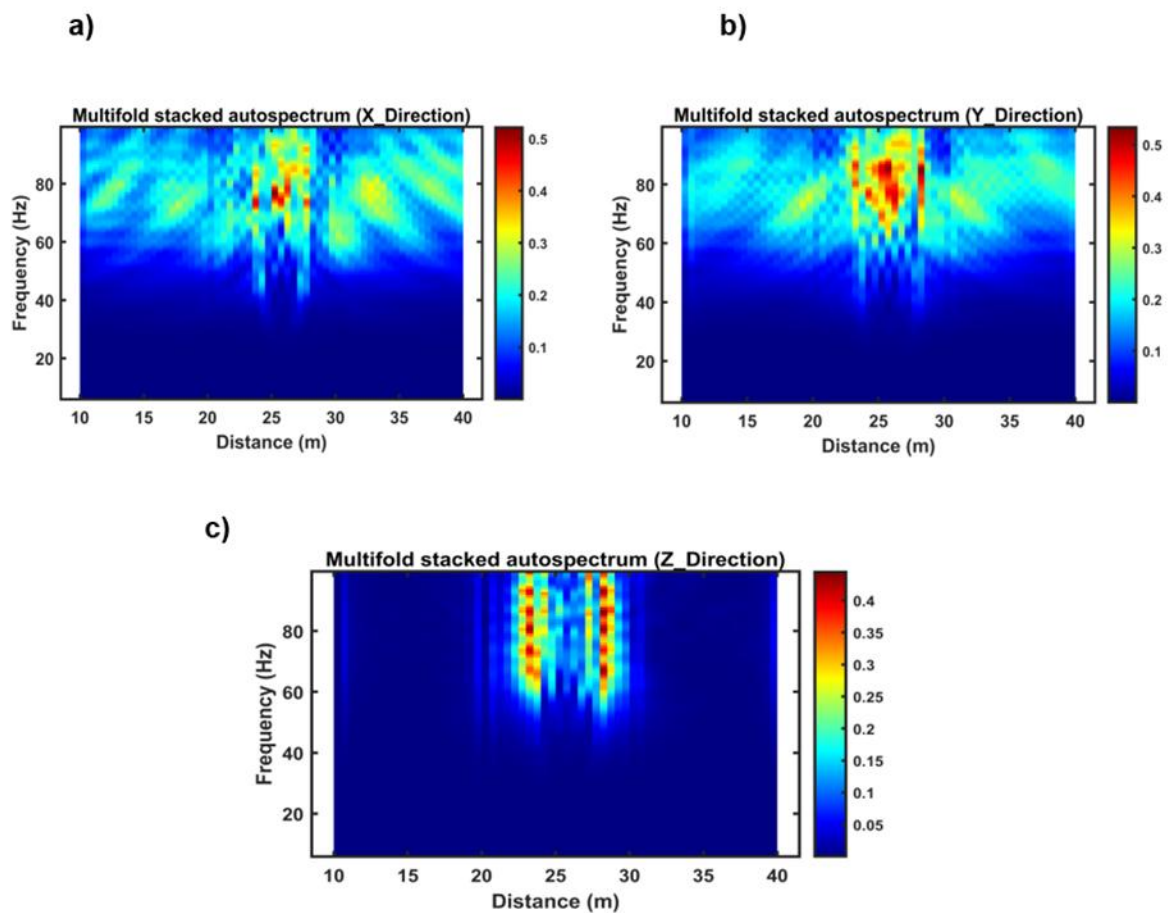
Figure 3-23: Multifold stacked autospectrum results for model A a) X-Component b) Y-Component c) Z-Component.
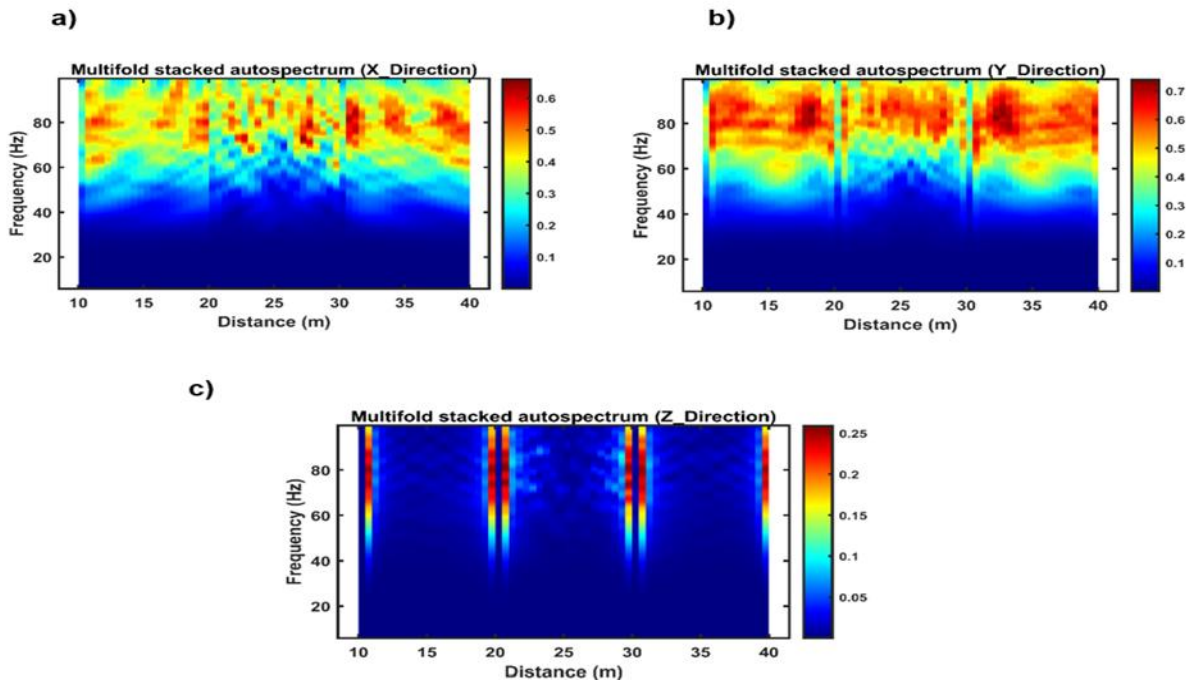
Figure 3-24: Multifold stacked autospectrum results for model B a) X-Component b) Y-Component c) Z-Component.
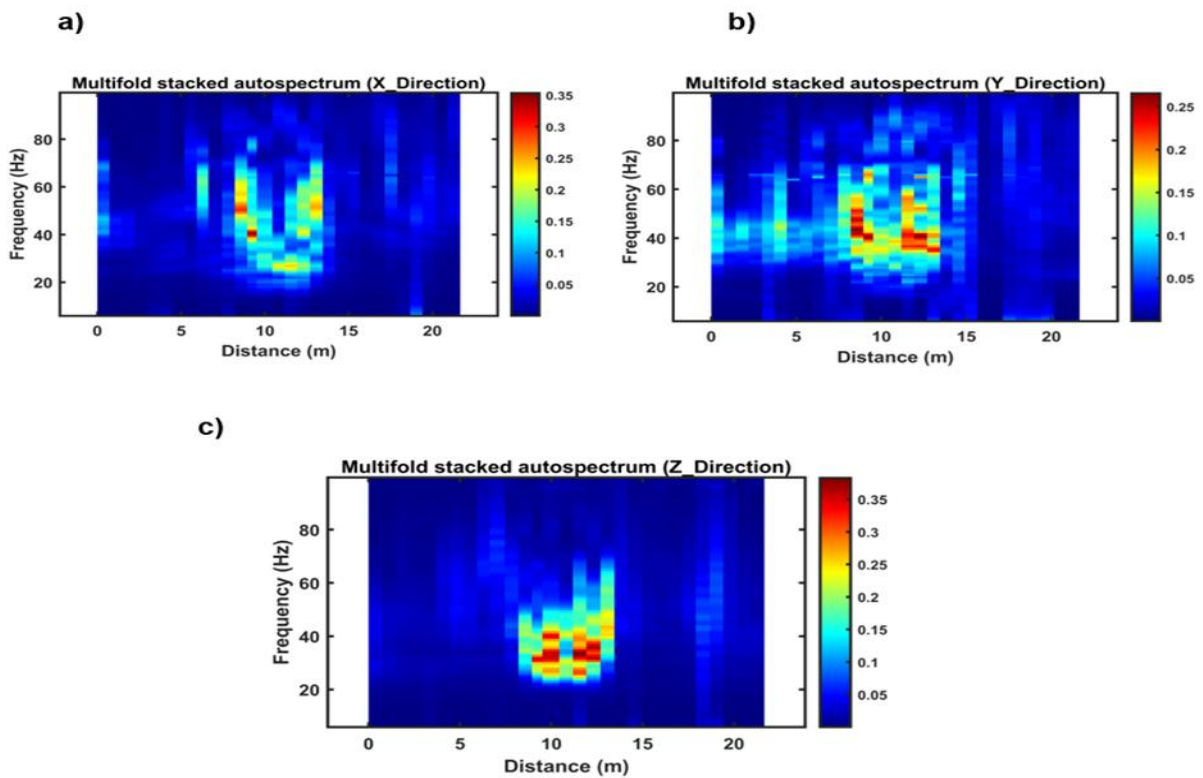
Figure 3-25: Multifold stacked autospectrum results for CNR site a) X-Component b) Y-Component c) Z-Component.

4   Chapter 4: Methodology

The surface wave attributes used in this study are based on several energy enhancement or attenuation parameters, and they have proved to be sensitive to lateral heterogeneities (Colombero et al., 2019). They are computed as a function of frequency and work for lateral identification of the position of the target. We show two methods to identify the depth of the target extent. The first is applied to a single component record and is based on the transformation of the frequency into wavelength and then into an estimate of the velocity. The second exploit the 3C and apply the spectral ratio method to estimate the depth. Both methods are applied to the autospectrum data and rely on the energy and energy decay exponent to define the lateral extent of the target.

4.1   1C data: pseudo-depth estimation

The method is based on two fundamental steps, the first step is aimed at selecting a frequency in the autospectrum image that corresponds to the bottom of the anomaly generated by the target, see Fig.3-22 for the CNR site. This frequency is then transformed into a wavelength thanks to the estimation of the SW dispersion curve in correspondence to the target. The wavelength is then transformed directly into a depth by applying the W/D method (Socco et al, 2017). To estimate the frequency that corresponds to the anomaly bottom, we implemented a method in the following called Energy Ratio Method.

4.1.1   Energy Ratio Method

We will introduce the concept of the energy ratio, which is the energy inside the target (energy inside the anomaly) over the energy inside the background. This energy ratio is computed using the autospectrum attribute, which shows the variations in energy distribution across different frequencies. The energy ratio ER is expressed by equation (3.5):

$$ER = \frac{ET_i(f)}{EB_i(f)} \qquad (3.5)$$

Where $ET_i(f)$ and $EB_i(f)$ are the energy inside the target and the background based on autospectrum attribute, respectively.

Where ETi (f) and $EB_i(f)$ are the energy inside the target and the background based on autospectrum attribute, respectively.

By plotting the energy ratio as a function of frequency along different axes, the first step of depth estimation starts by selecting a specific frequency, and this value corresponds to the boundary of the amplitude anomaly generated by the target. By analyzing Fig.4-1 for synthetic model A along X component, we observe that the energy ratio increases reaching a peak (first maximum) and then declines beyond that frequency. We will call this frequency the peak energy frequency (PEF), which will be transformed into wavelength using the corresponding phase velocity extracted from the dispersion curve (DC) Fig.4-2.
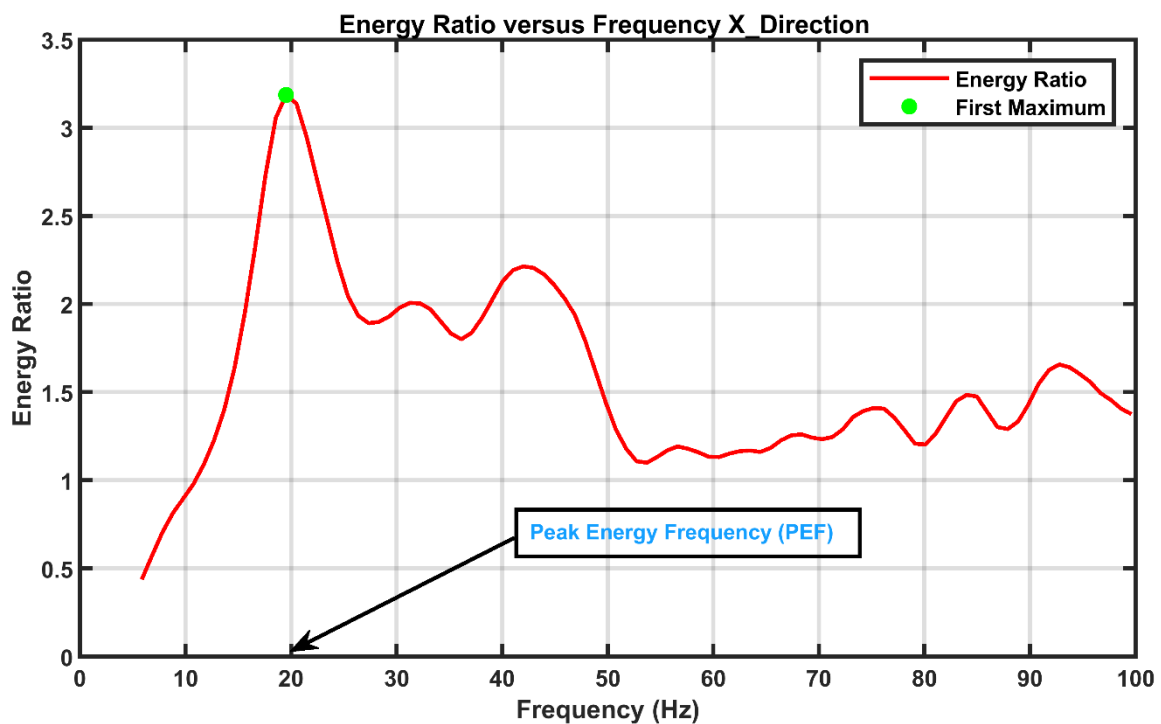
Figure 4-1: Energy Ratio versus Frequency.

4 METHODOLOGY
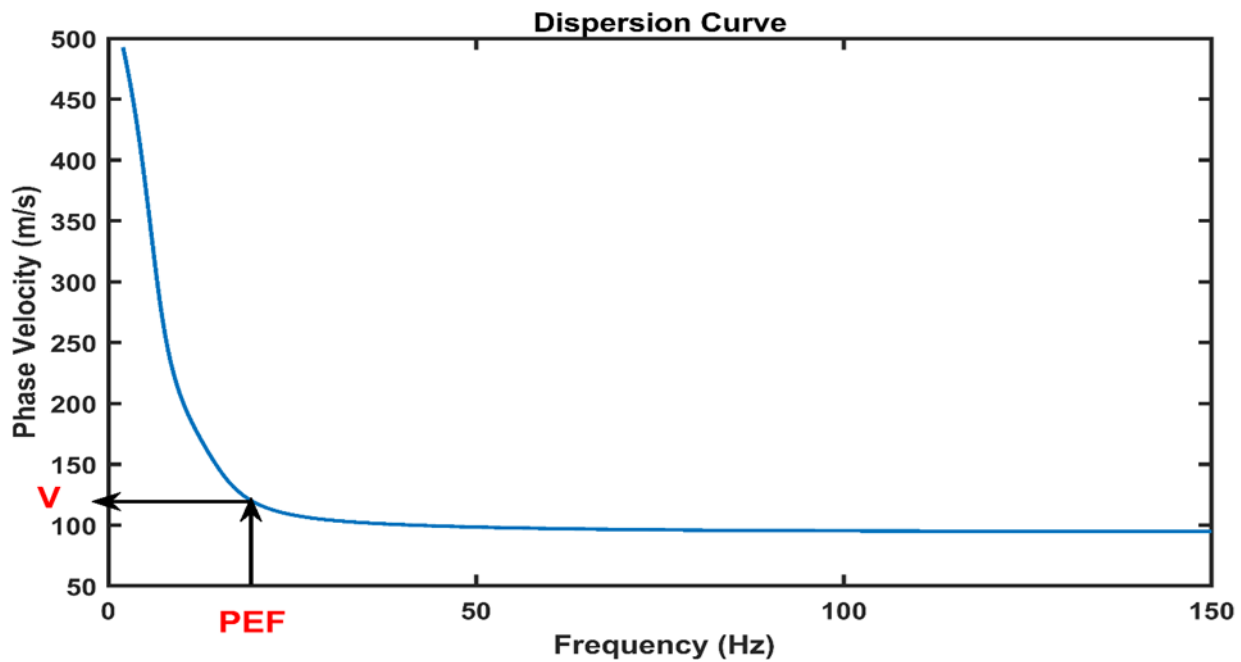
Figure 4-2: Dispersion curve (frequency – phase velocity).

After that, the extracted phase velocity value (V) is employed in the following equation (3.6), which illustrates the relationship between wavelength and phase velocity.

$$\lambda = \frac{V}{f}, \qquad\qquad (3.6)$$

Where λ is the wavelength in m, V is the phase velocity in m/s, and f is the frequency in Hz.

The wavelength will be retrieved in the same way for the Y component and the component combination (XY), the combination of components will be calculated as the average between the two different components (X and Y). Then, we will apply the following methods to estimate the depth of the target.

1) Pseudo-Depth approach:

Once the wavelength corresponding to the bottom of the anomaly has been identified using the energy ratio and the dispersion curve, the wavelength must be transformed into a depth. For this scope, two approaches have been implemented and tested.

 We have applied a very simple relationship suggested by literature (see section 2.2.2) and simply identified the depth as half the wavelength ($\lambda/2$) according to the following equation (3.7):

$$Z = \frac{\lambda}{2} \qquad\qquad (3.7)$$

Where Z is the depth of the target in m, and λ is the wavelength in m.

2) **Wavelength/Depth (W/D) Relationship:**

      The wavelength-to-depth (W/D) relationship Fig.4-3 establishes one to one correspondence among the investigation depth and wavelength. It is based on the search of the pair of wavelength and depth for which the phase velocity of the Rayleigh wave is equal to the time average S-wave velocity (Socco et al., 2017). This principle directly converts the DC to a depth-dependent model and differs from the conventional inversion methods, which are complicated and often non-unique. So, by carrying the conversion, we can estimate the depth of the bottom of the anomaly directly transforming the wavelength into depth. In our work, we will use this relationship by applying the obtained wavelength for all components and then converting it to depth. The target depth will be equal to the mean of the depths for all components estimated using W/D relationship.
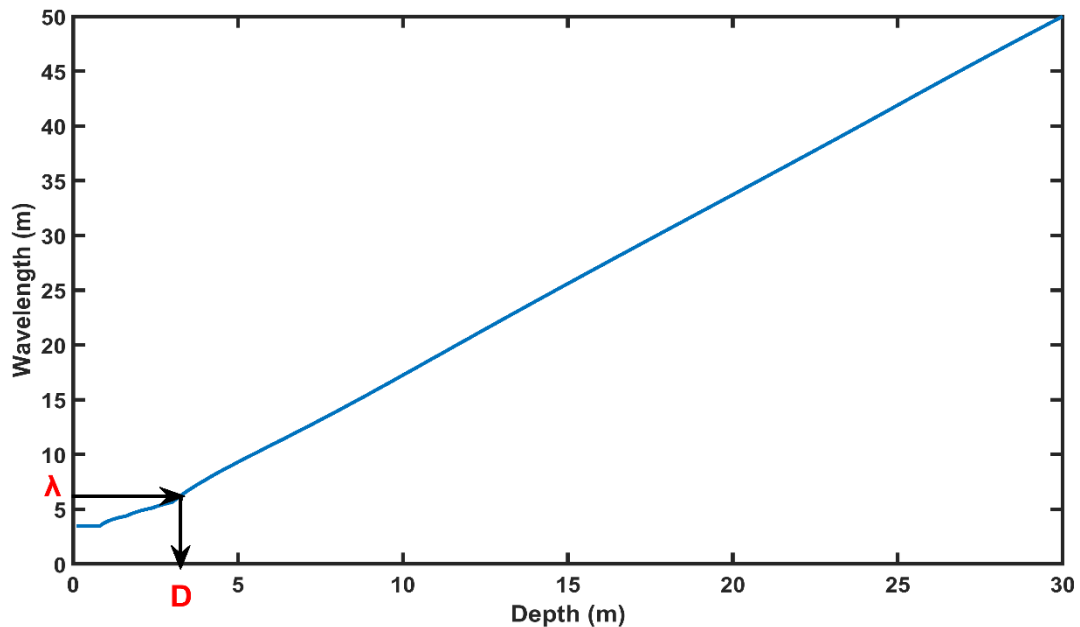
Figure 4-3: W-D relationship estimated following the approach of (Socco et al., 2017).

41

4 METHODOLOGY

4.2 3C data: H/V Ratio Method

Horizontal to vertical spectral ratio was first it proposed by Nogoshi and Igarashi (1971) and then widely spread by Nakamura (1989) and then will be known as (Nakamura's technique). This technique has gained popularity over the past years since it is an inexpensive method and can be applied to regions of low seismicity. This technique consists in estimating the ratio between the Fourier amplitude spectra of the horizontal (H) to vertical (V) components of the ambient noise vibrations recorded at one single station

This ratio is described in the following equation (3.7), in which the square root of the squared autospectrum values for the horizontal components (X and Z components) over the autospectrum along the vertical (Y component).

$$H / V = \frac{\sqrt{(G_i^2)x + (G_i^2)z}}{(G_i^2)y} \qquad (3.7)$$

The autospectrum for all components is a function of frequency, and in that case, now we can plot the H/V ratio versus frequency Fig.4-4. This method is robust in the case of a stiff layer over a half space layer, and in our situation, is more complicated since the background will affect the results. We used the synthetic data to evaluate the H/V method performance in correspondence to the target and the data evidenced several peaks of resonance frequency. The first peak is at low frequency and is related to the growing velocity at greater depth in the background. There is a second resonance peak which is instead compatible with the contrast of impedance due to the bottom of the target. Therefore, for the depth estimation we will use the second peak in the H/V plot.
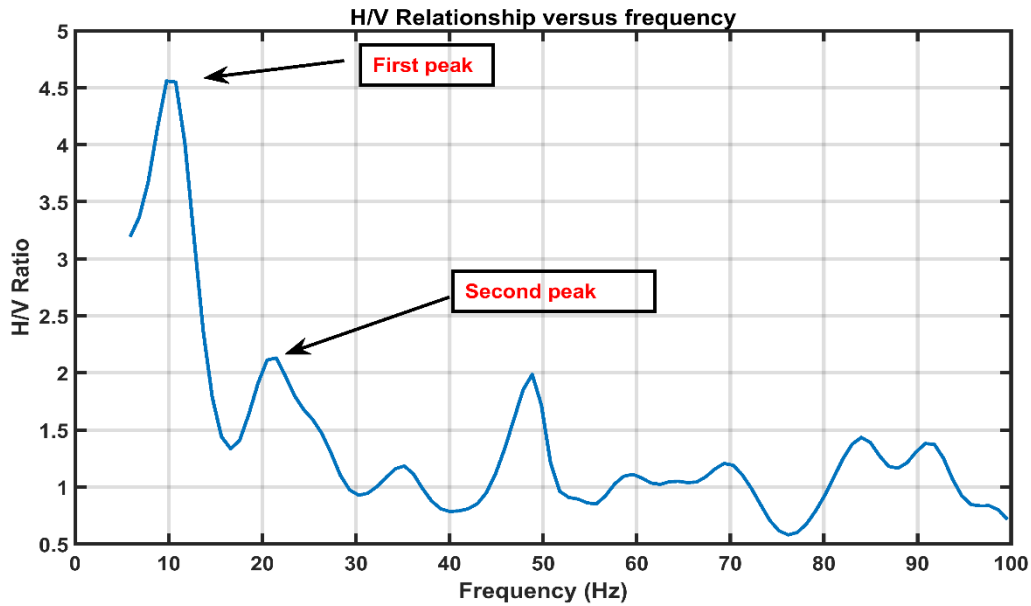
Figure 4-4: H/V ratio versus frequency.

The frequency value obtained at the second peak will be the input to the dispersion curve (DC) in which the phase velocity will be received Fig.4-5.
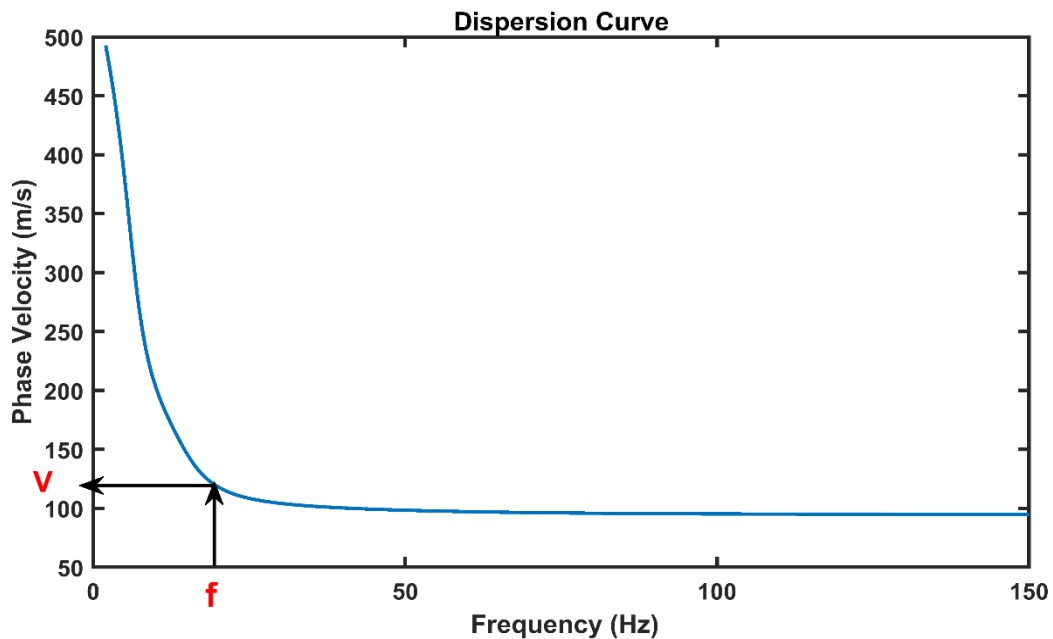
Figure 4-5: Dispersion curve (frequency – phase velocity).

Then, by using the relationship between the phase velocity and wavelength equation (3,6) we can determine the wavelength (λ) and we will apply the pseudo-depth approach to determine the depth of the anomaly, which will be equal to $\lambda/2$.

5 Chapter 5: Results & Discussion

5.1 Depth Estimation Using Energy Ratio Method

In the following, we apply the energy ratio concept for two synthetic models and a CNR site. The results for estimating the depth will be shown in the following plots. In addition, to ensure the best frequency band selection for reliable prediction. The energy attribute is estimated using a filtered frequency range along different components (X, Y, and Z) based on the study described in Appendix A.

Figure 5-1 illustrates the relationship between the energy ratio as a function of frequency in the X, Y, and XY components for model A. In the X component (red) the energy ratio increases and reaches a peak of 3.2 at a frequency of 20 Hz, and this will be the Peak energy frequency (PEF). Beyond that first peak, the energy ratio decreases as the frequency increases. For Y component (blue) the energy ratio shows a similar trend, increasing to around 3.9 at 23 Hz before decreasing as the frequency rises. For the XY combination components (green), the energy ratio increases to a maximum peak of 3.2 at 21.5 Hz, followed by a steep decline and minor oscillations at higher frequencies
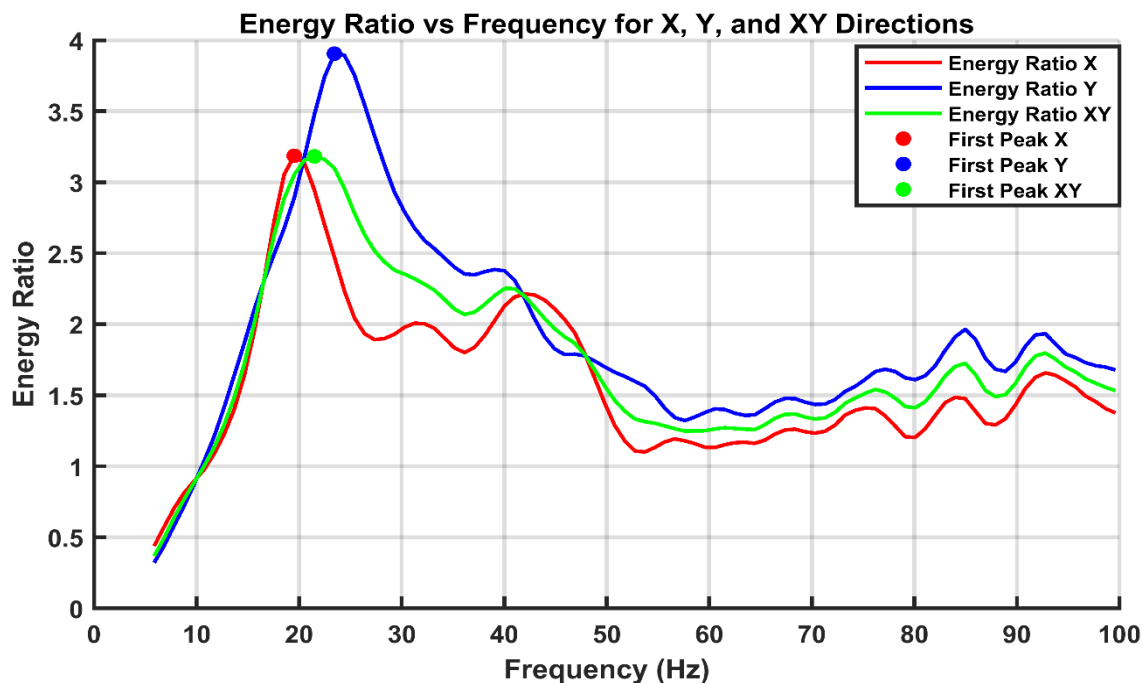
Figure 5-1: Energy Ratio versus Frequency for model A.

5 RESULTS & DISCUSSION

These differences indicate that the model displays distinct frequencies and energy distribution along each component. Our target is to estimate the depth of the anomaly; using the frequency value obtained at the peak (PEF), then by referring to section 4.1, we can estimate the depth of the lateral heterogeneity. The wavelength along the X component is 5.8 m, the Y component is 4.8 m, and the wavelength for the XY component is 5.3 m.

Table 1 summarizes the estimated depth for all components for model A.

Component	First Peak by ER (-)	PEF (Hz)	Wavelength (m)	Pseudo-Depth (m)	Estimated Depth by (W/D) Relationship
X	3.2	20	5.8	2.9	3.1
Y	3.9	23	4.8	2.4	2.3
XY	3.2	21.5	5.3	2.7	2.8

True Depth = 3.1 m

Table 1: Results obtained for synthetic model A.

The energy ratio method plot for synthetic model B Fig.5-2 shows the same trend as synthetic model A. The same procedure was applied to estimate the depth of the target, which has a true depth of 5 m. The results for depth estimation regarding synthetic model B are summarized in Table 2.

5 RESULTS & DISCUSSION

Figure 5-2:Energy Ratio versus Frequency for model B.

Component	First Peak by ER (-)	PEF (Hz)	Wavelength (m)	Pseudo-Depth (m)	Estimated Depth by (W/D) Relationship
X	1.6	17	9.7	4.9	3.4
Y	1.9	13	12.3	6.2	5.6
XY	1.4	15	11.6	5.8	5.3

True Depth = 5 m

Table 2: Results obtained for synthetic model B.

Figures 5-3 shows the results obtained for energy ratio method plot for CNR site. The same procedure is used to estimate the anomaly depth for the CNR Site, and the estimated depths are summarized in Table 3.

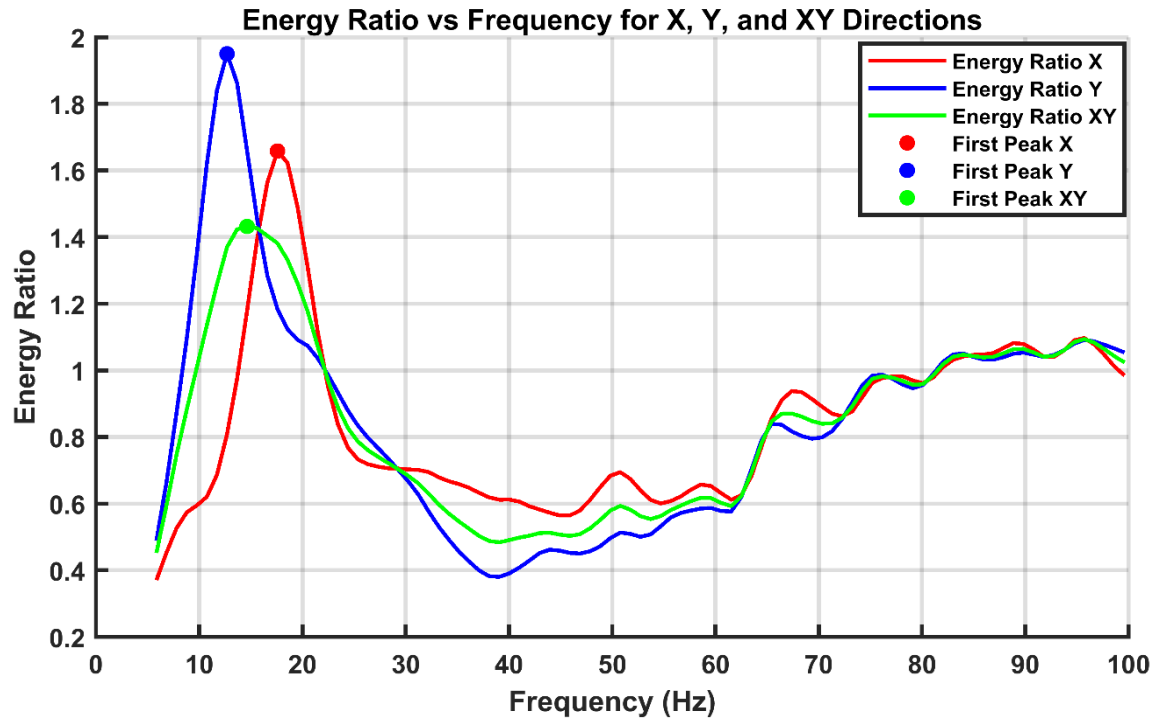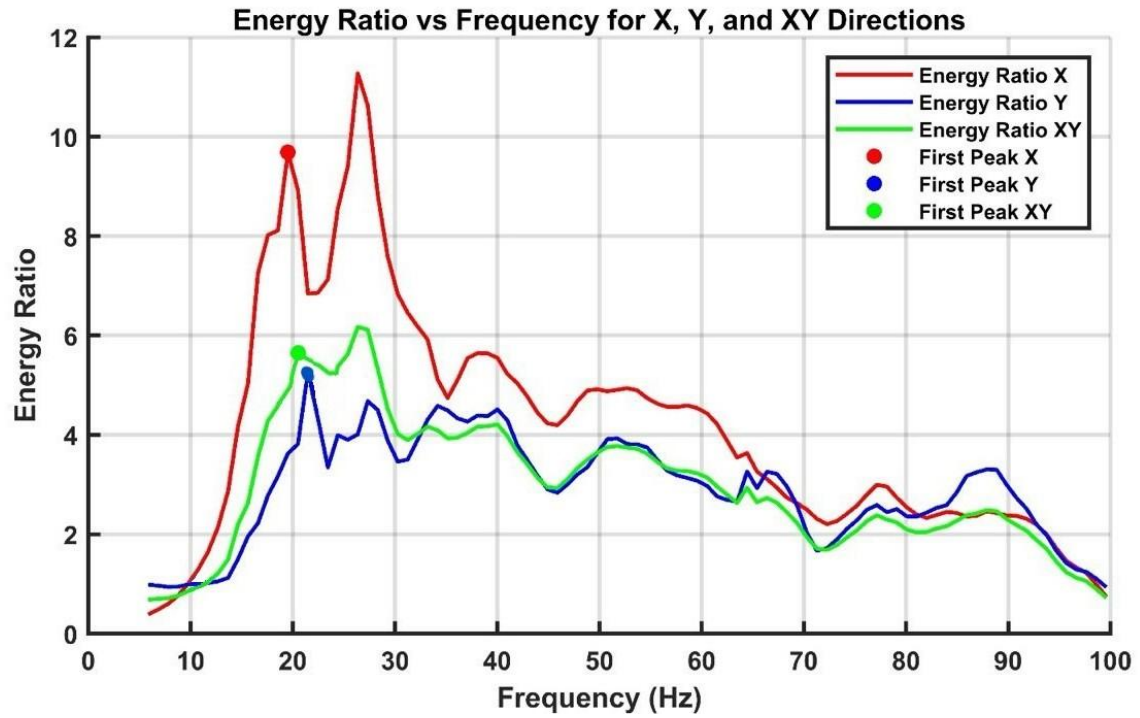*Figure 5-3: Energy Ratio versus Frequency for CNR site.*

Component	First Peak by ER (-)	PEF (Hz)	Wavelength (m)	Pseudo-Depth (m)	Estimated Depth by (W/D) Relationship
X	8	20	5.9	3	3.1
Y	4.3	22	5.2	2.6	2.5
XY	5.9	21	5.6	2.8	2.9

True Depth = 2.5 m

Table 3: Results for CNR site.

5 RESULTS & DISCUSSION

5.2 Depth Estimation Using H/V Ratio Method

Figures 5-13 and 5-14 show the H/V spectral ratio method plots for synthetic models A and B, respectively. The plots show the H/V ratio versus frequency, and the second peak will be picked at 21 Hz for model A and 20 Hz for model B. Figure 5-15 refers to the CNR site with a second peak of 20 Hz. The wavelength will be 6.4 m for model A and 7.6 m for model B. For CNR site the wavelength obtained will be equal to 7.2 m. Therefore, the depth of the target is 3.2 m for model A and for model B we find underestimation, with a depth of 3.8 m. At the CNR site, there's a depth overestimation reaching 3.6 m.
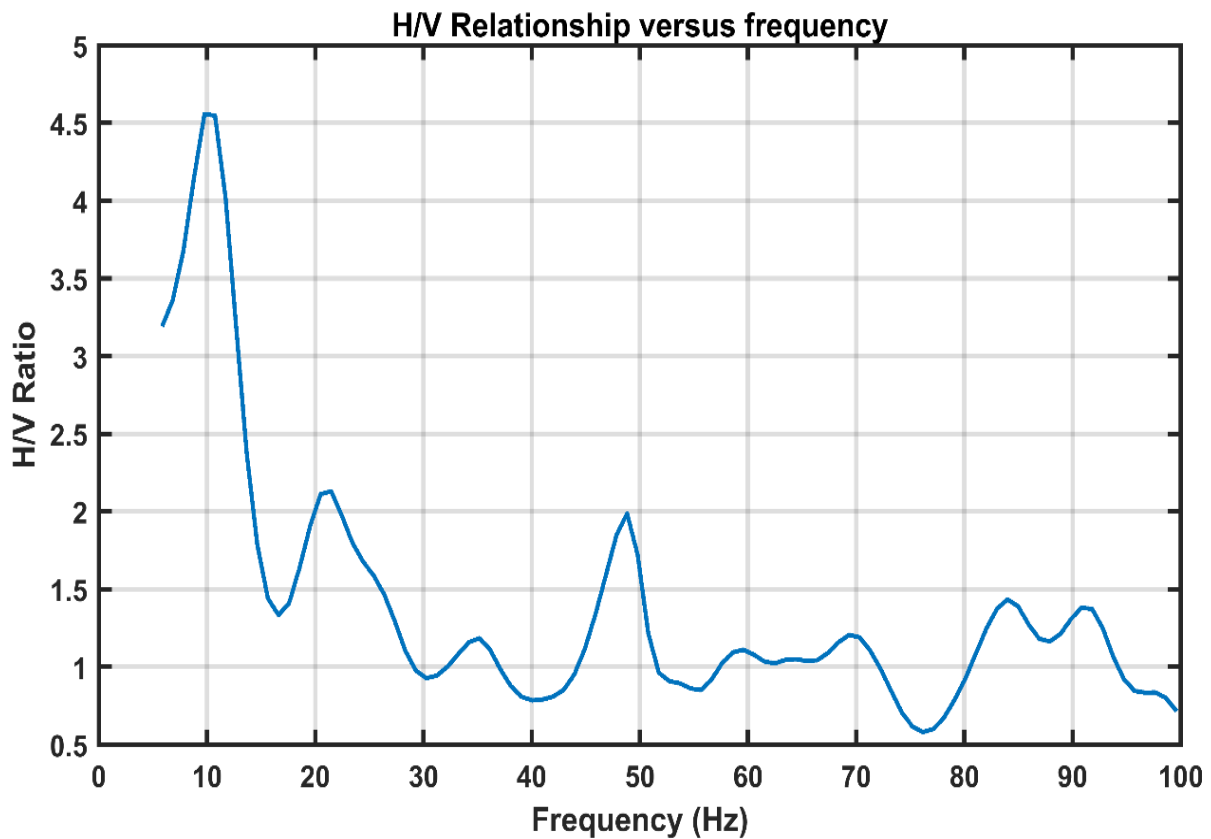

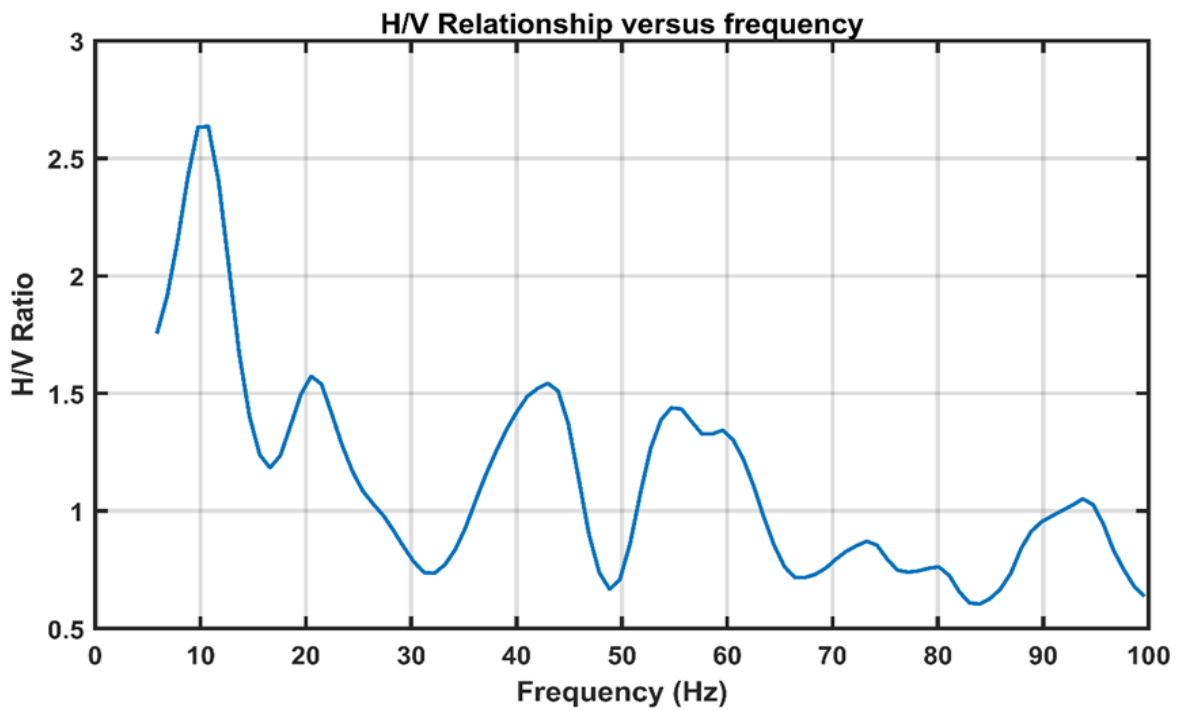*Figure 5-4:H/V spectral ratio method versus frequency for model A.*

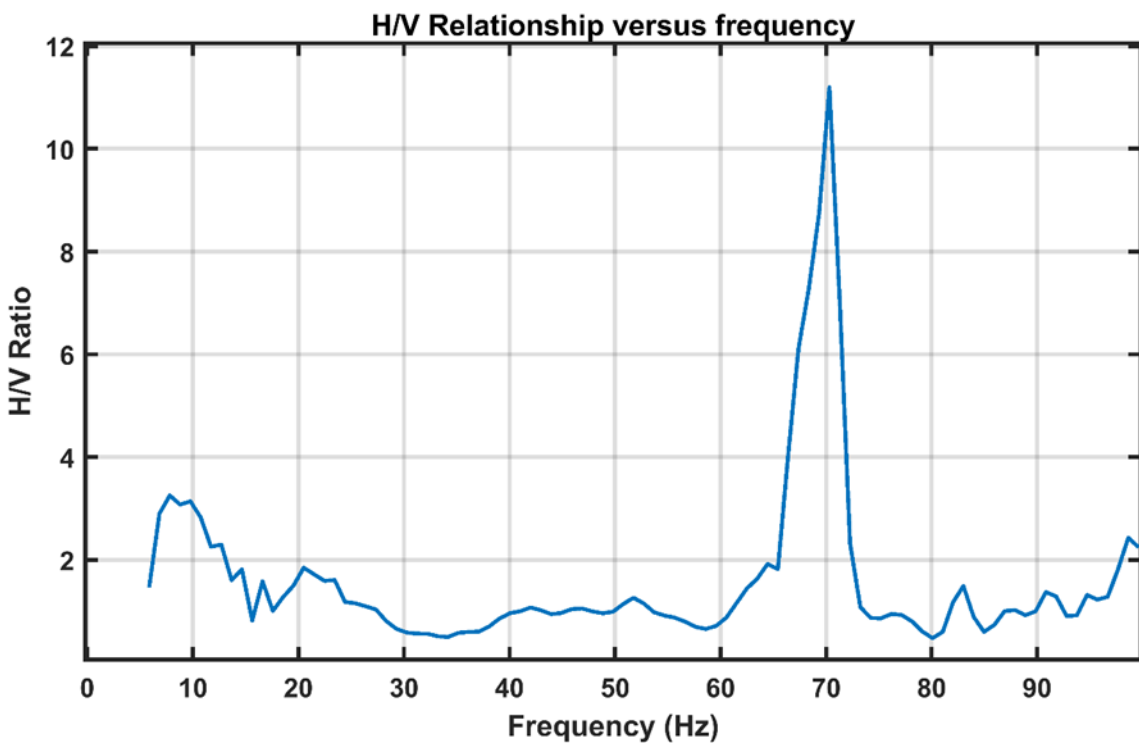*Figure 5-5:H/V spectral ratio method versus frequency for model B.*

Figure 5-6: H/V spectral ratio method versus frequency for CNR site.

5 RESULTS & DISCUSSION

5.3 Depth Estimation comparison

Table 3 summarizes all the estimated depths and the comparison between all the methods used. By using the pseudo-depth approach after selecting the PEF to estimate the depth of target, the results indicate relatively accurate estimation for model A, the lowest error +0.1 m and the relative error reaches 3 %. While the results indicate higher overestimation of the depth for both model B and the CNR site. The error will be +0.8 m and a relative error of 16 % for model B, and for CNR site, the error is +0.3 m and a relative error of 12 %.

By using the W/D approach after selecting the PEF to estimate the depth of target, the results indicate relatively accurate estimation for model B, the lowest error with +0.3 m and the relative error reaches 6 %, and for CNR site the error is +0.4 m and a relative error of 16%. Regarding model A, the results indicate an underestimation of the depth. The error is -0.3 m and a relative error of 9 % for model A.

On the other hand, by using the pseudo-depth approach to estimate the depth through H/V spectral ratio, the results indicate both depth overestimation and underestimation. For model A, the lowest error +0.1 m and the relative error reaches 3% and For CNR site, the overestimation of depth will be revealed with the error reaching +1.1 m and a relative error of 44 %. While the results indicate an underestimation of the depth for model B, the error is -1.2 m and a relative error of 24%.

Model	True Depth (m)	Pseudo Depth (m) based on ER method	Estimated Depth by W/D (m)	Pseudo Depth based on H/V method (m)
A	3.1	3.2	2.8	3.2
B	5	5.8	5.3	3.8
CNR Site	2.5	2.8	2.9	3.6

Table 4: Depth estimation analysis: pseudo depth, W/D, and H/V Method for Models A, B, and CNR Site.

The pseudo-depth approach and W/D relationship based on ER method are reliable as it balances accuracy and consistency. The relative errors were lower for all models. While the pseudo-depth based on the H/V technique shows higher relative errors, especially for model B and the CNR site.

6 Chapter 6: Conclusion

This thesis highlighted the ability of SW attributes to identify and assess the depth of sharp lateral heterogeneities. We established the effectiveness of SW attributes in identifying lateral heterogeneities using energy, energy decay exponent, and autospectrum. We developed the energy ratio method to estimate the depth of low-velocity anomalies. This method uses multi-component data to enable wavelength identification for depth computations using pseudo-depth and W/D relationship. Two synthetic models (A & B) and a real-world case study (CNR test site) were used to evaluate the techniques.

The estimated depth by using the pseudo-depth based on energy ratio method aligns well with the actual depths. The estimated depths were 3.2 m for Model A, 5.8 m for Model B, and 2.8 m for the CNR site, closely matching the actual anomaly depths of 3.1 m, 5.0 m, and 2.5 m, respectively.The W/D approach also demonstrated strong performance, particularly for Model B, where the estimated depth (5.3 m) was very close to the actual depth (5.0 m). For the CNR site, the W/D method estimated a depth of 2.9 m, slightly overestimating by 0.4 m (16% error). However, for Model A, the W/D method slightly underestimated the depth. Despite these variations, the W/D relationship remains a reliable method, particularly for deeper targets. It has to be stressed though that W/D relation was estimated using the dispersion curves of the retrieved from the vertical component and this may have introduced errors in the process.

The H/V spectral ratio method produced mixed results. It approximately estimates the depth for Model A (error +0.1 m), but underestimated Model B (error -1.2 m, 24%) and overestimated the CNR site (error +1.1 m, 44%). These discrepancies suggest that while the H/V method may be effective in specific conditions, it is less consistent across different models.

Finally, this thesis illustrates that the energy ratio method establishes an effective basis for depth estimation. Improving its accuracy will further enhance the reliability of depth estimations since the pseudo-depth and W/D computations rely directly on the extracted wavelengths. This thesis prepared the ground for advancements in near-surface geophysics related to geotechnical engineering and environmental hazard assessment.

7 References

[1] Bergamo, P., Boiero, D., & Socco, L. V. (2012). Retrieving 2D structures from surface-wave data by means of space-varying spatial windowing. Geophysics, 77(4), EN39–EN51. https://doi.org/10.1190/geo2012-0031.1

[2] Bergamo, P., & Socco, L. V. (2014). Detection of sharp lateral discontinuities through the analysis of surface-wave propagation. Geophysics, 79(4), EN77–EN90. https://doi.org/10.1190/geo2013-0314.1

[3] Bohlen, P. J., Scheu, S., Hale, C. M., McLean, M. A., Migge, S., Groffman, P. M., & Parkinson, D. (2004). Non-native invasive earthworms as agents of change in northern temperate forests. Frontiers in Ecology and the Environment, 2(8), 427–435. https://doi.org/10.1890/1540-9295(2004)002[0427:nieaao]2.0.co;2

[4] Boiero, D., Bergamo, P., Bruno Rege, R., & Socco, L. V. (2011). Estimating surface-wave dispersion curves from 3D seismic acquisition schemes: Part 1 — 1D models. Geophysics, 76(6), G85–G93. https://doi.org/10.1190/geo2011-0124.1

[5] Bohlen, T., De Nil, D., Köhn, D., & Jetschny, S. (2015). SOFI3D - Seismic modeling with finite differences: 3D - acoustic and viscoelastic version (User Guide). Karlsruhe Institute of Technology, Geophysical Institute.

[6] Braile, L. W. (2006). Seismic Waves and the Slinky: A Guide for Teachers.

[7] Chopra, S., & Marfurt, K. J. (2005). Seismic attributes — A historical perspective. Geophysics, 70(5), 3SO-28SO. https://doi.org/10.1190/1.2098670

7 REFERENCES

[8] Colombero, C., Comina, C., & Socco, L. V. (2019). Imaging near-surface sharp lateral variations with surface-wave methods — Part 1: Detection and location. Geophysics, 84(6), EN93–EN111. https://doi.org/10.1190/geo2019-0149.1

[9] Foti, S., Lai, C. G., Rix, G. J., & Strobbia, C. (2017). Surface wave methods for near-surface site characterization. CRC Press.

[10] Hévin, G., Abraham, O., Pedersen, H. A., & Campillo, M. (1998). Characterization of surface cracks with Rayleigh waves: A numerical model. NDT & E International: Independent Nondestructive Testing and Evaluation, 31(4), 289–297. https://doi.org/10.1016/s0963-8695(98)80013-3

[11] Ikeda, T., & Tsuji, T. (2016). Surface wave attenuation in the shallow subsurface from multichannel–multishot seismic data: A new approach for detecting fractures and lithological discontinuities. Earth, Planets, and Space: EPS, 68(1). https://doi.org/10.1186/s40623-016-0487-0

[12] Lane, J. W., Jr, White, E. A., Steele, G. V., & Cannia, J. C. (2008). Estimation of bedrock depth using the horizontal-to-vertical (H/V) ambient-noise seismic method. Symposium on the Application of Geophysics to Engineering and Environmental Problems 2008.

[13] Nasseri-Moghaddam, A., Cascante, G., & Hutchinson, J. (2005). A new quantitative procedure to determine the location and embedment depth of a void using surface waves. Journal of Environmental & Engineering Geophysics, 10(1), 51–64. https://doi.org/10.2113/jeeg10.1.51

[14] Park, C. B., Miller, R. D., & Xia, J. (1998). Imaging dispersion curves of surface waves on multi-channel record. SEG Technical Program Expanded Abstracts 1998.

7 REFERENCES

[15] Safitri, D., Nainggolan, T. B., & Manik, H. M. (2020). Common reflection surface methods in low fold coverage seismic data of complex marine geological structures. IOP Conference Series. Earth and Environmental Science, 429(1), 012032. https://doi.org/10.1088/1755-1315/429/1/012032

[16] Samyn, K., Bitri, A., & Grandjean, G. (2012). Imaging near-surface feature using cross-correlation analysis of multi-channel surface-wave data. Near Surface Geophysics. https://doi.org/10.3997/1873-0604.2012007

[17] Schwenk, J. T., Sloan, S. D., Ivanov, J., & Miller, R. D. (2016). Surface-wave methods for anomaly detection. Geophysics. https://doi.org/10.1190/geo2015-0356.1

[18] Sloan, S. D., Miller, R. D., Ivanov, J., Moran, M. L., & Cudney, H. H. (2016). Depth estimation of voids using backscattered surface waves. SEG Annual Meeting. https://doi.org/10.1190/seg-2016-13961352

[19] Sripanich, Y., & Fomel, S. (2017). Fast time-to-depth conversion and interval velocity estimation with weak lateral variations. SEG Annual Meeting. https://doi.org/10.1190/seg-2017-17647817

[20] Socco, L. V., Jongmans, D., Boiero, D., Stocco, S., Maraschini, M., Tokeshi, K., & Hantz, D. (2010). Geophysical investigation of the Sandalp rock avalanche deposits. Journal of Applied Geophysics, 70(4), 277–291. https://doi.org/10.1016/j.jappgeo.2009.12.005

[21] Strobbia, C., & Foti, S. (2006). Multi-offset phase analysis of surface wave data (MOPA). Journal of Applied Geophysics, 59(4), 300–313. https://doi.org/10.1016/j.jappgeo.2005.10.009

[22] Takanashi, M. (2014). Influence of small-scale lateral heterogeneity on seismic velocity analysis and time-to-depth conversion. International Petroleum Technology Conference. https://doi.org/10.2523/IPTC-18099-MS

7 REFERENCES

[23]   Zerwer, A., Polak, M. A., & Santamarina, J. C. (2005). Detection of surface breaking cracks in concrete members using Rayleigh waves. Journal of Environmental & Engineering Geophysics, 10(3), 295–306. https://doi.org/10.2113/jeeg10.3.295

8 Appendix A

Here, we will show the results for the energy attribute for two synthetic models (A & B) and the CNR site for different frequencies.

8.1.1 Example 1: Synthetic Model A

By knowing the source positions for model A at 10 m,20 m,30 m, and 40 m and the anomaly boundaries between 23 m and 28 m at lower frequencies, especially 5 Hz Fig.8-1, we can see the source effects without any changes within the anomaly. As the frequency increases to 16 Hz Fig.8-2, the energy value increases and becomes more concentrated in the anomaly zone, especially for both X and Y components. Meanwhile, in the Z component, the energy values remain minimal within the anomaly zone. These patterns suggest that the fault boundaries are affected first in both X and Y components, while the Z component is not yet observed.

When the frequency reached 21 Hz Fig.8-3 and 35 Hz Fig.8-4, the effect of boundaries was observed in all components. The boundaries of the anomaly were first seen in both the X and Y components and later in the Z component. For the X and Y components, the boundaries and shape of the anomaly were observed at 21 Hz, and for the Z component at 35 Hz.

As the frequency increases and when it reaches 65 Hz Fig.8-5, the energy values become irregular, and the boundaries for an anomaly are not well defined or stable like in the previous frequency bands. So, the energy analysis for a frequency of 65 Hz is characterized by inconsistency, which confirms that the frequency values used to estimate the depth of the anomaly are reasonable.
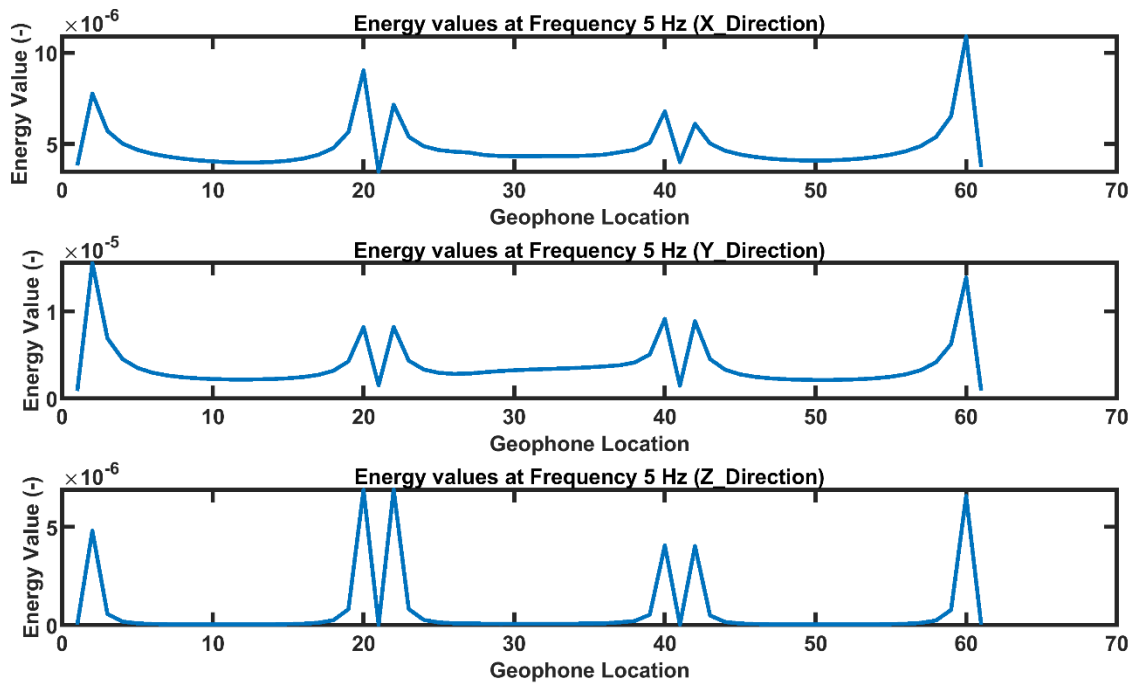
8 APPENDIX

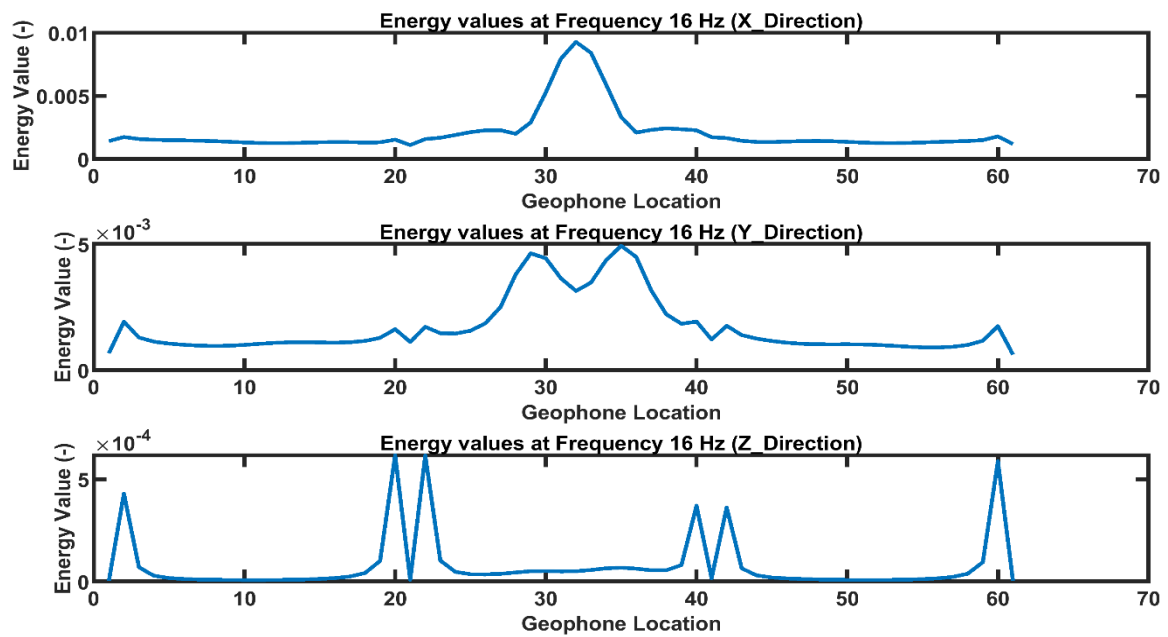*Figure 8-1: Energy attribute analysis at 5 Hz for model A.*

Figure 8-2: Energy attribute analysis at 16 Hz for model A.
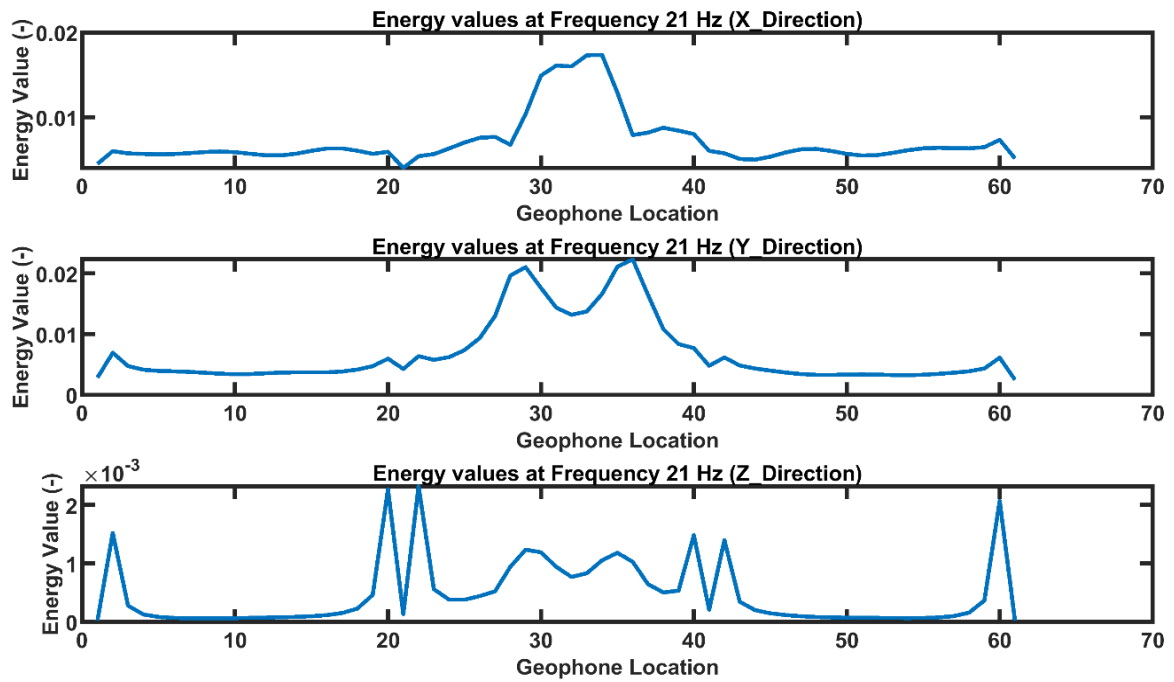
Figure 8-3: Energy attribute analysis at 21 Hz for model A.
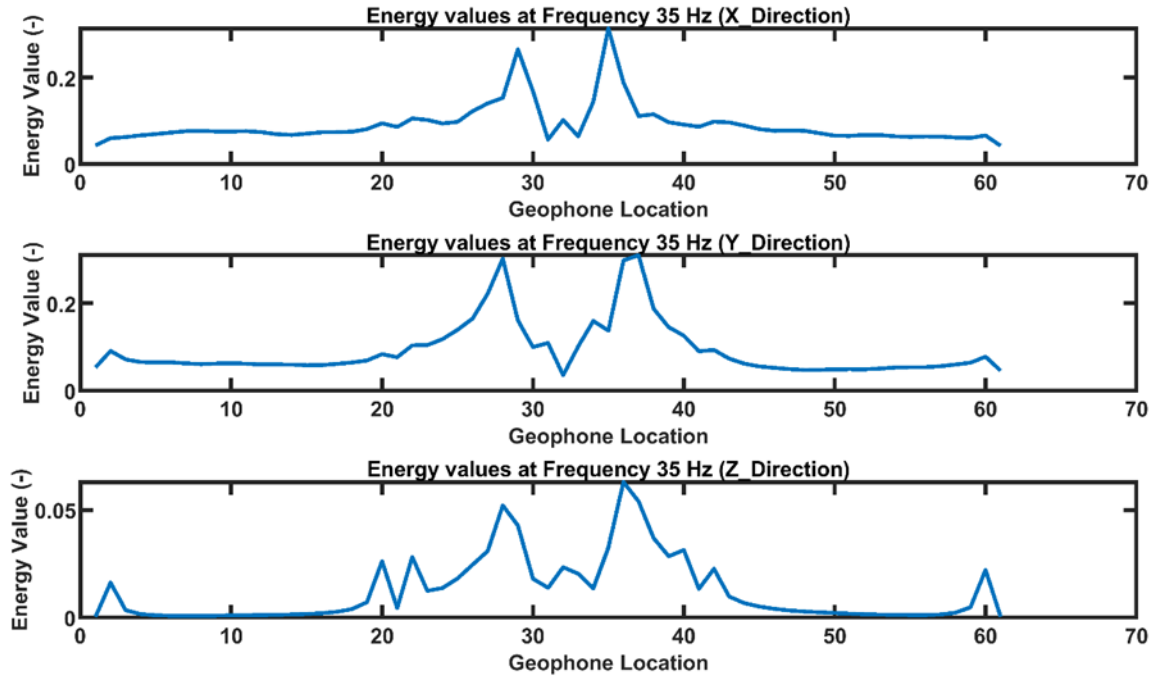

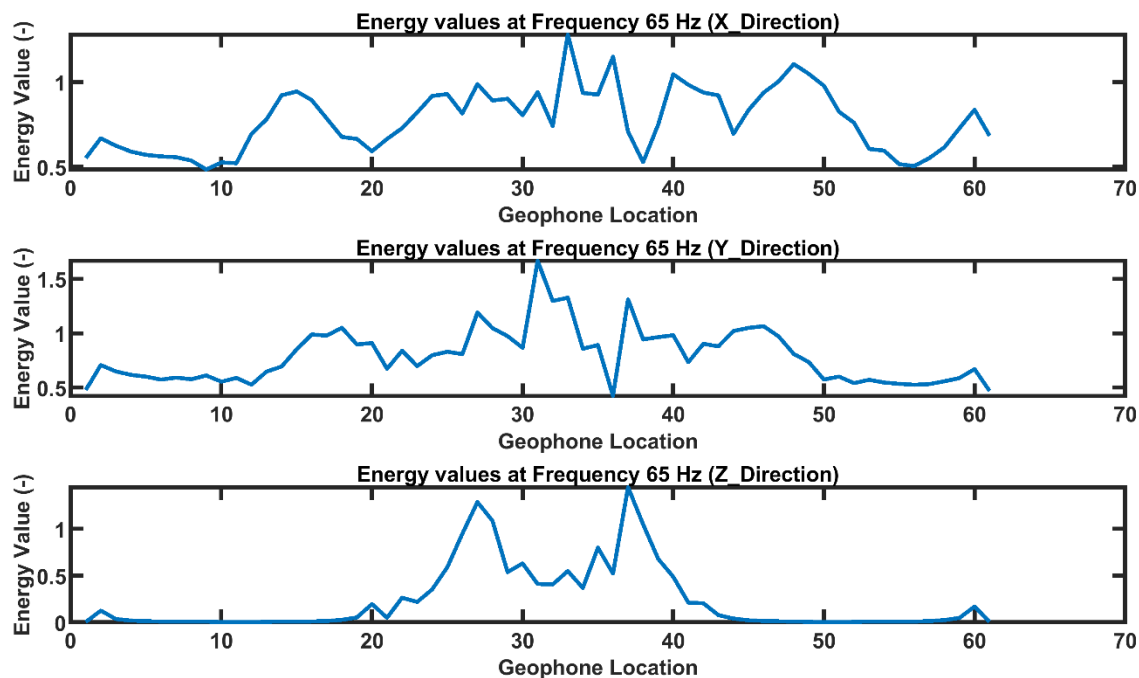*Figure 8-4:Energy attribute analysis at 35 Hz for model A*

Figure 8-5: Energy attribute analysis at 65 Hz for model A.

8.1.2 Example 2: Synthetic model B

The source positions for model B at 10 m,20 m,30 m, and 40 m and the anomaly boundaries between 23 m and 28 m, at lower frequencies, especially 5 Hz Fig.8-6, we can see the source effects without any changes within the anomaly. As the frequency increases to 13 Hz Fig.8-7 and 17 Hz Fig.8-8, the energy value increases and becomes more concentrated in the anomaly zone, especially for both X and Y components. Meanwhile, in the Z component, the energy values remain minimal within the anomaly zone. These patterns suggest that the fault boundaries are affected first in both X and Y components while along Z component is not yet observed.

As the frequency increases and when it reaches 60 Hz Fig.8-9, the energy values become irregular, and the boundaries for an anomaly are not well defined or stable like in the previous frequency bands. So, the energy analysis for a frequency of 60 Hz is characterized by inconsistency, which confirms that the frequency values used to estimate the depth of the anomaly are reasonable.
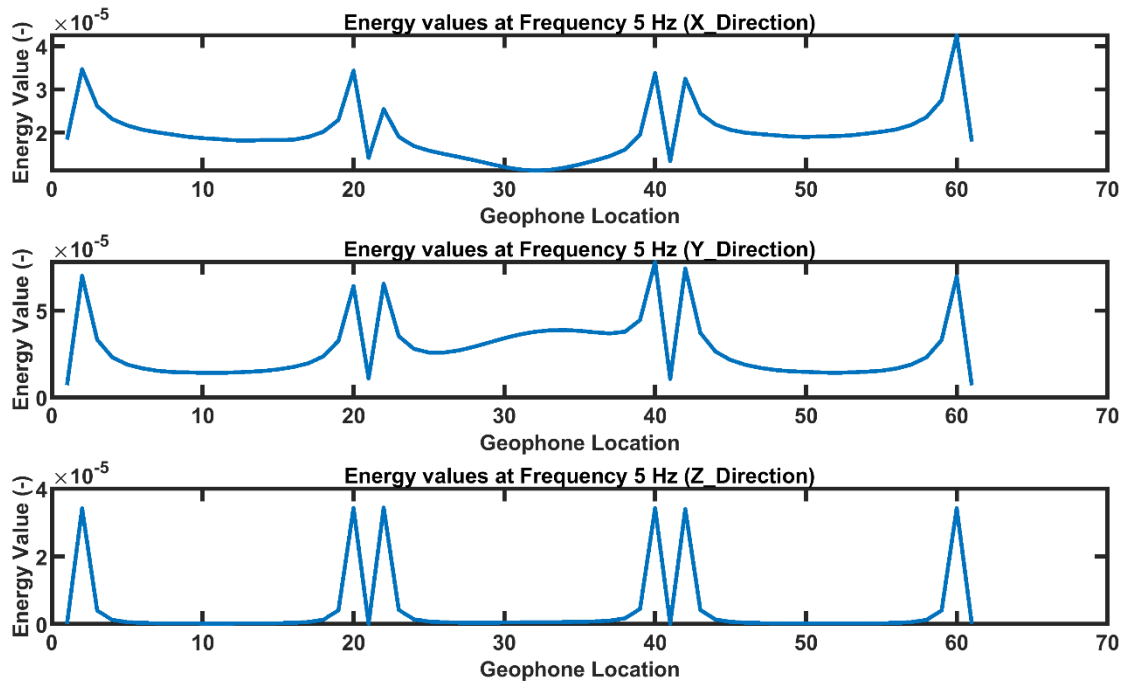
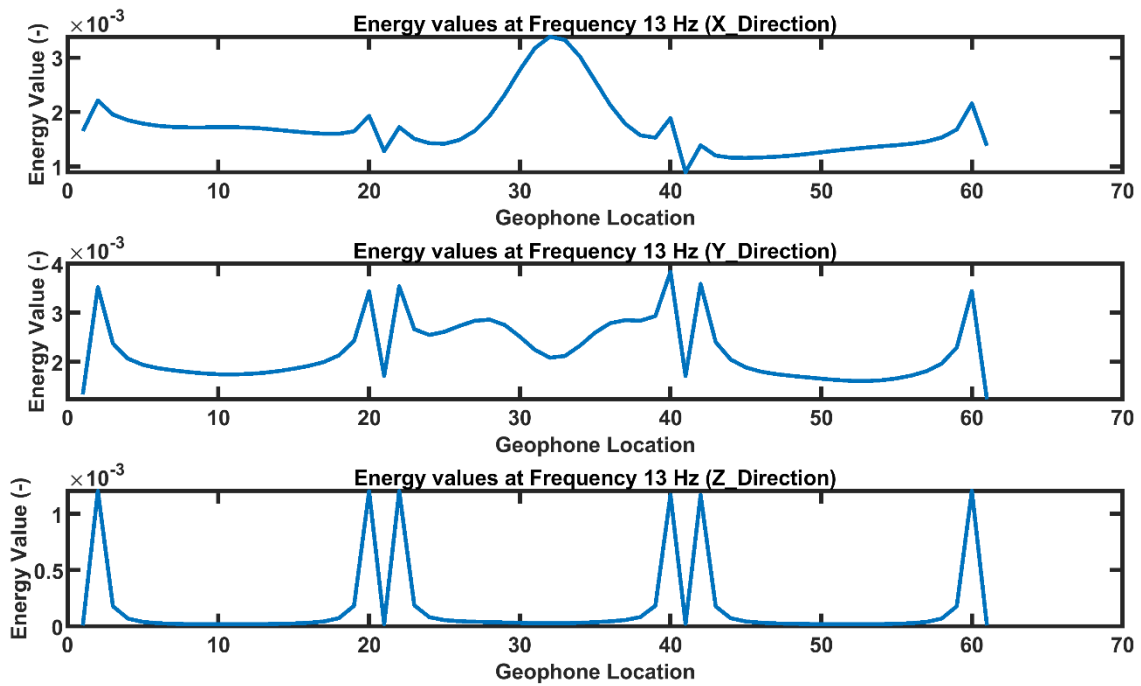*Figure 8-6: Energy attribute analysis at 5 Hz for model B.*

Figure 8-7: Energy attribute analysis at 13 Hz for model B.
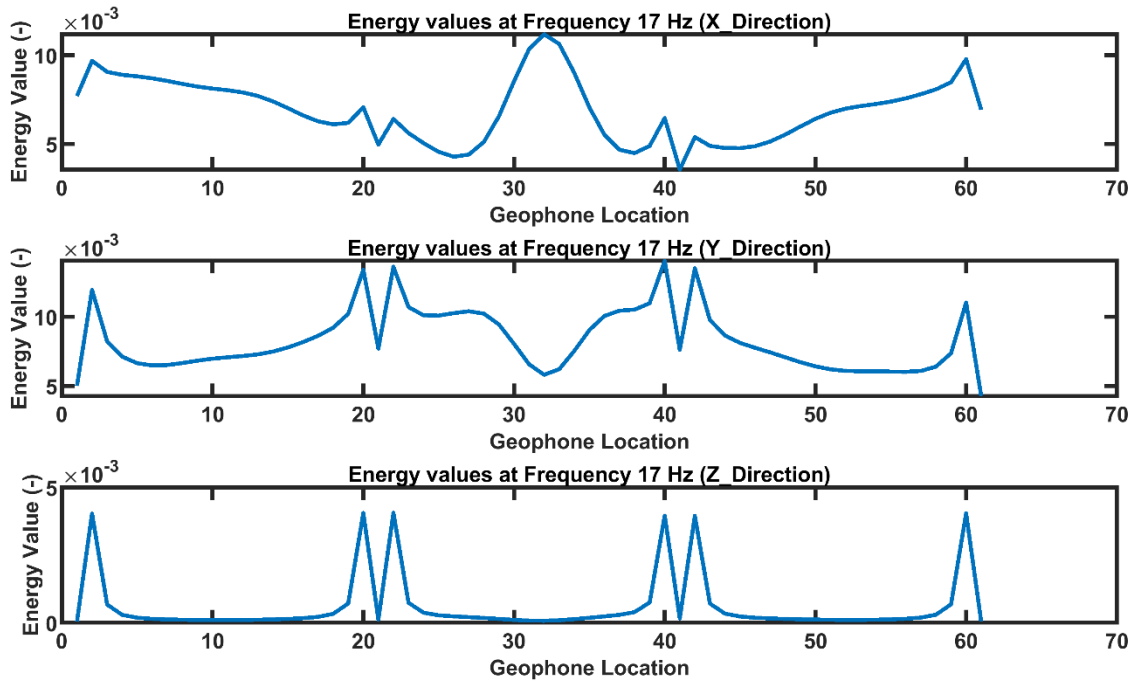
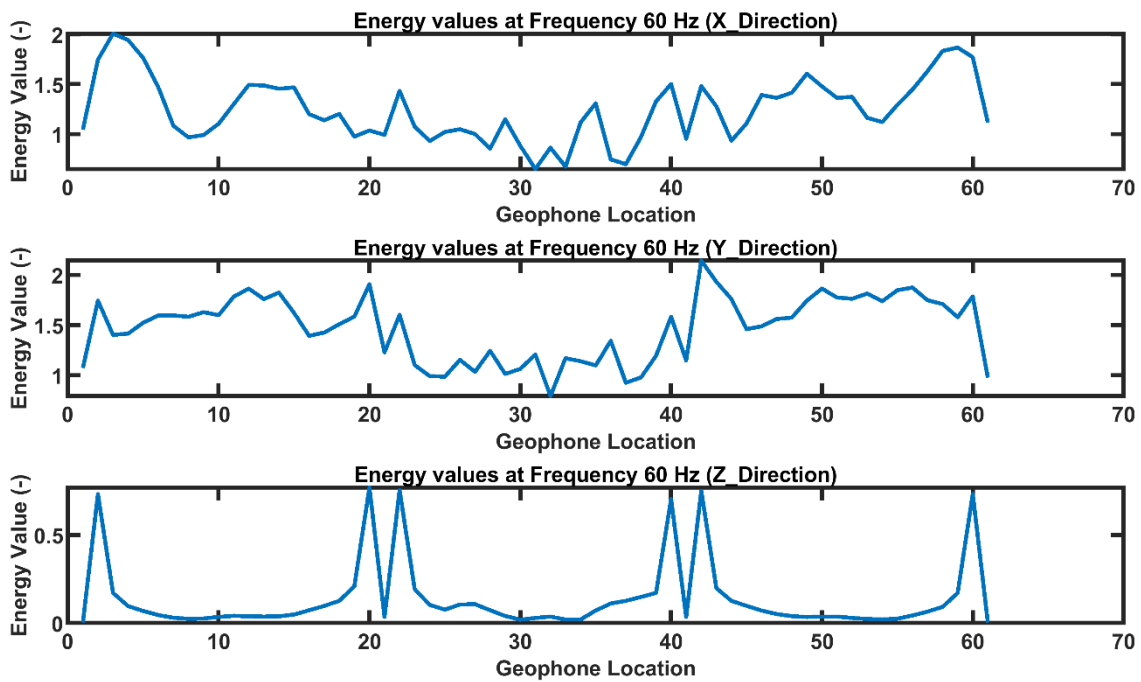*Figure 8-8: Energy attribute analysis at 17 Hz for model B.*

Figure 8-9: Energy attribute analysis at 60 Hz for model B.

8.1.3 Example 3: CNR Site

For the CNR site, the anomaly boundaries are between 8 m and 13 m;at lower frequencies, especially 9 Hz Fig.8-10; we can see the source effects without any changes within the anomaly, and this effect is not the same as for synthetic models. As the frequency increases to 20 Hz Fig.8-11 and 26 Hz Fig.8-12, the energy value increases and becomes more concentrated in the anomaly zone in all components.

As the frequency increases, reaching 65 Hz Fig.8-13, the energy values become irregular, and the boundaries of an anomaly are not well defined or stable like in the previous frequency bands. So, the energy analysis for a frequency of 60 Hz is characterized by inconsistency, which confirms that the frequency values used to estimate the depth of the anomaly are reasonable.
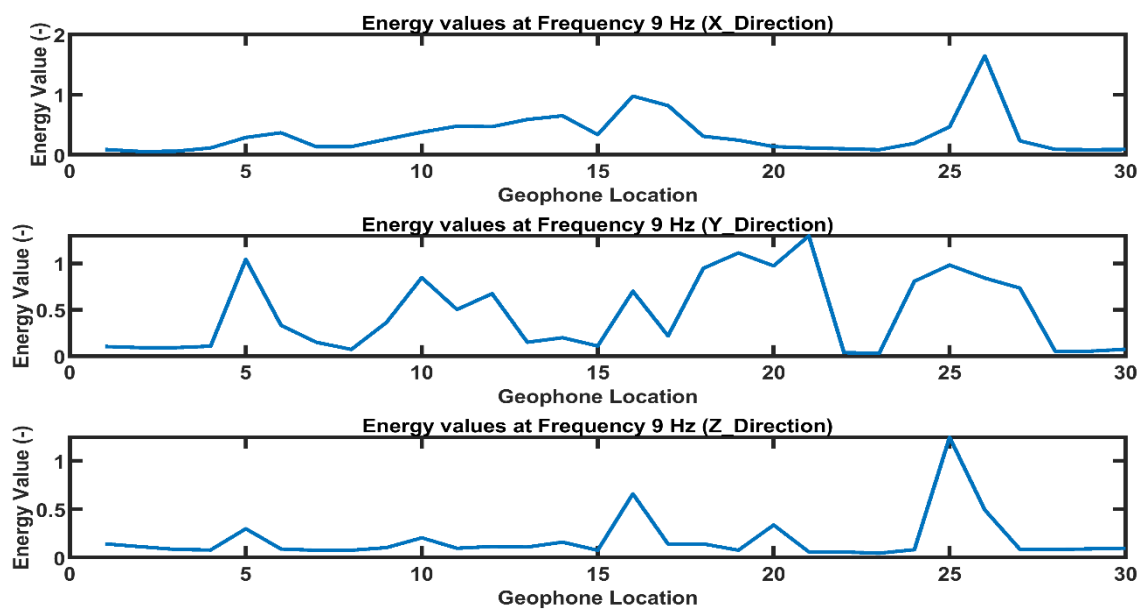

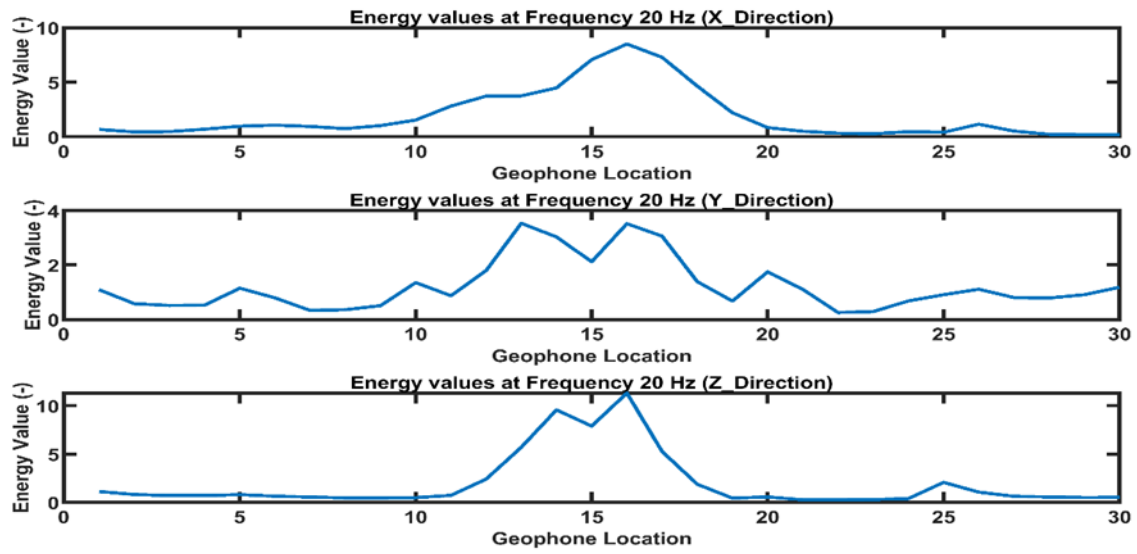*Figure 8-10: Energy attribute analysis at 9 Hz for CNR site.*

Figure 8-11: Energy attribute analysis at 20 Hz for CNR site.

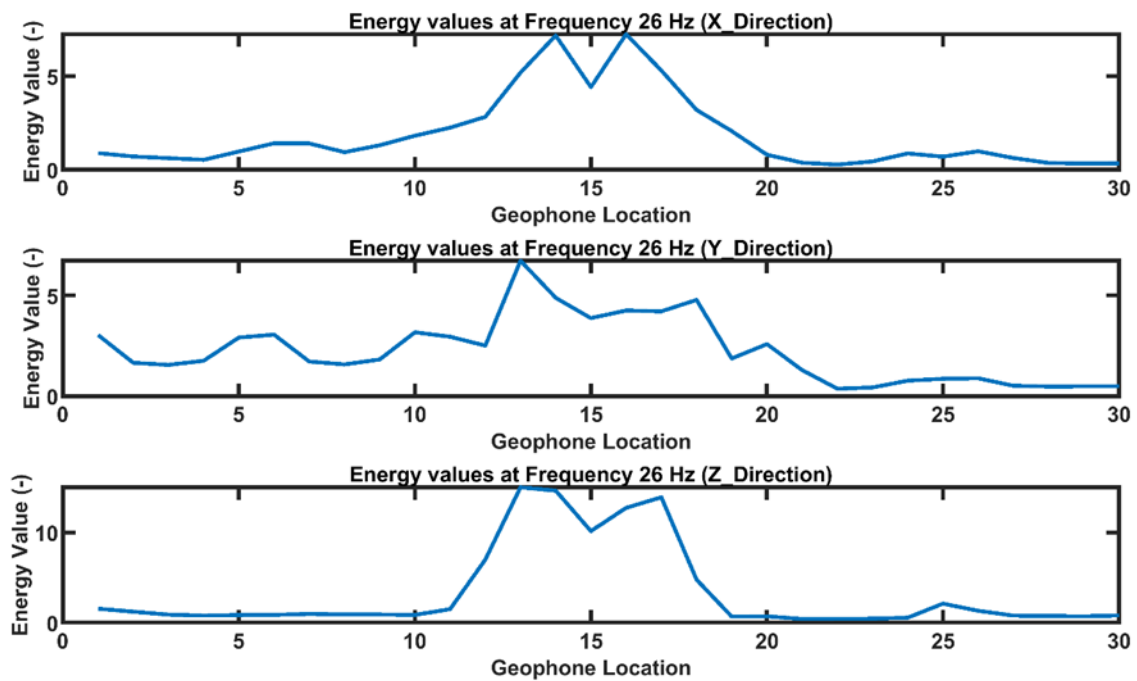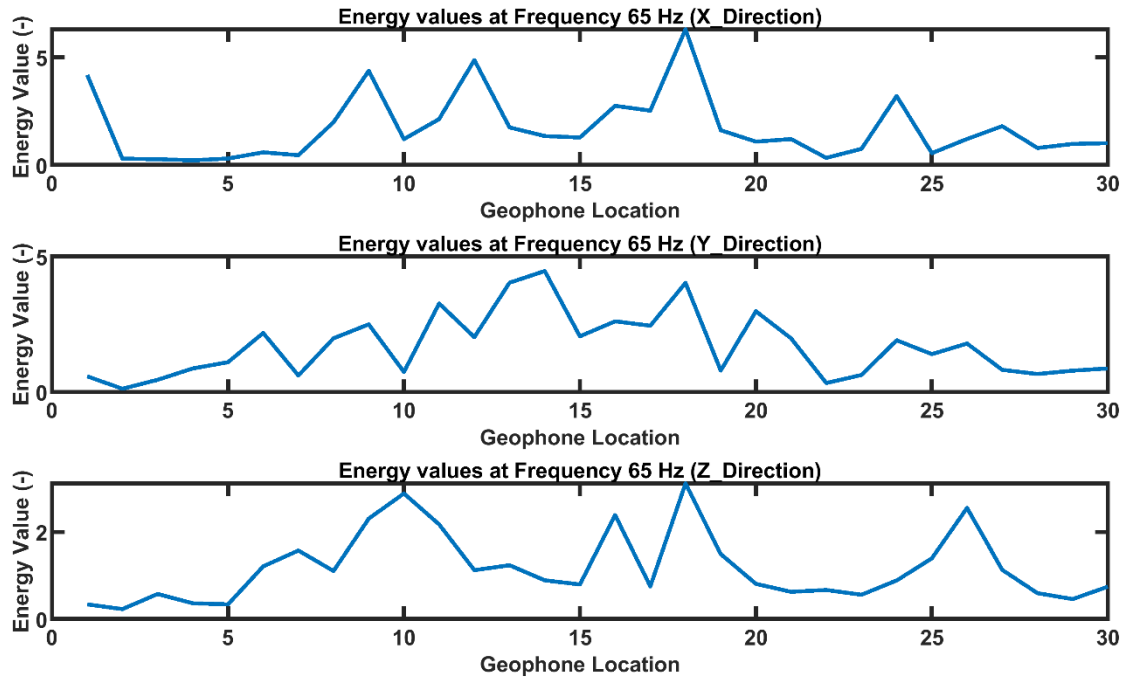*Figure 8-12:Energy attribute analysis at 26 Hz for CNR site.*

Figure 8-13: Energy attribute analysis at 65 Hz for CNR site.